A Review of NEST Models, and Their Application to Improvement of Particle Identification in Liquid Xenon Experiments

M. Szydagis,[1,*] J. Balajthy,[2,3] G.A. Block,[1,4] J.P. Brodsky,[5] E. Brown,[4] J.E. Cutter,[2,6] S.J. Farrell,[7] J. Huang,[2,8] E.S. Kozlova,[9,10] C.S. Liebenthal,[7] A. Manalaysay,[2,11] D.N. McKinsey,[11,12] K. McMichael,[4] M. Mooney,[13] J. Mueller,[13] K. Ni,[8] G.R.C. Rischbieter,[1] M. Tripathi,[2] C.D. Tunnell,[7] V. Velan,[12] M.D. Wyman,[1] Z. Zhao,[8] and M. Zhong[8]

[1]*Department of Physics, University at Albany, State University of New York, 1400 Washington Ave., Albany, NY 12222, USA*
[2]*Department of Physics, University of California Davis, One Shields Ave., Davis, CA 95616, USA*
[3]*Sandia National Laboratories, Livermore, CA 94550, USA*
[4]*Department of Physics, Applied Physics and Astronomy, Rensselaer Polytechnic Institute, Troy, NY 12180, USA*
[5]*Lawrence Livermore National Laboratory, 7000 East Ave., Livermore, CA 94551, USA*
[6]*Deepgram, Mountain View, CA 94103, USA*
[7]*Department of Physics and Astronomy, Rice University, Houston, TX 77005, USA*
[8]*Department of Physics, University of California San Diego, La Jolla, CA 92093, USA*
[9]*Institute for Theoretical and Experimental Physics Named by A.I. Alikhanov of National Research Centre "Kurchatov Institute," 117218 Moscow, Russia*
[10]*Moscow Engineering Physics Institute (MEPhI), National Research Nuclear University 115409 Moscow, Russia*
[11]*Lawrence Berkeley National Laboratory, 1 Cyclotron Rd., Berkeley, CA 94720, USA*
[12]*Department of Physics, University of California Berkeley, Berkeley, CA 94720, USA*
[13]*Department of Physics, Colorado State University, Fort Collins, CO 80523, USA*

This paper discusses microphysics simulation of interactions in liquid xenon, the medium in many leading rare-event physics searches, and describes experimental observables useful to understanding detector performance. Scintillation and ionization yield distributions for signal and background are presented using the Noble Element Simulation Technique (NEST), a toolkit based on experimental data and simple, empirical formulae. NEST models of light and charge production as a function of particle type, energy, and electric field are reviewed, as well as of energy resolution and final pulse areas. After vetting of NEST against raw data, with several specific examples pulled from XENON, ZEPLIN, LUX / LZ, and PandaX, we interpolate and extrapolate its models to draw new conclusions on the properties of future detectors (*e.g.*, XLZD's), in terms of the best possible discrimination of electron(ic) recoil backgrounds from a potential nuclear recoil signal, especially WIMP dark matter. We discover that the oft-quoted value of 99.5% discrimination is overly conservative. NEST shows that another order of magnitude improvement (99.95% discrimination) can be achieved with a high photon detection efficiency ($g_1 \sim 15-20\%$) at reasonably achievable drift fields of 200-350 V/cm.

Keywords: WIMP dark matter direct detection, 2-phase LXe TPCs, simulations / models

I. INTRODUCTION

For the past ∼15 years, the leading results from dark matter searches labeled as "direct detection" have come from detectors based on the principle of the dual-phase TPC (Time Projection Chamber) with the main detection medium being a noble liquid [1]. Detectors utilizing liquid xenon (LXe) have in particular produced the most stringent cross-section constraints, for spin-independent (SI) as well as spin-dependent (SD) neutron-nucleon interactions possible for WIMPs (Weakly Interacting Massive Particles), leading dark matter candidates. More recently, LXe usage has also led to WIMP limits using different EFT (Effective Field Theory) operators, for mass-energies O(5 GeV) out to several TeV [2]. EFTs extend the set of allowable operators, beyond the standard SI and SD, thus allowing for searches at higher recoil energies. Unrelated to dark matter, electron-recoil searches in the MeV regime have set the best constraints on $0\nu\beta\beta$ decay [3], and led to observing double electron capture [4].

To interpret results from past, present, and future experiments, across different energy regimes, a reliable MC (Monte Carlo) simulation is necessary, for experimentalists and theorists alike. Recent works (not counting LUX, the originator of NEST) demonstrating the reliability of NEST, the cross-disciplinary, detector-agnostic MC software used in this work, include [5–8], going beyond LXe. Demonstrations have included prediction of new results with little to no tuning. As multi-tonne-scale TPCs have commenced data collection, improved MC techniques will not only assist in limit setting, but will be needed to extract mass and cross section in case of a WIMP discovery. In either scenario, or for designing a new TPC, predicting performance on key metrics such as dark matter background discrimination, the focus of this work, is needed; its contradictory historical definitions will be reviewed.

* Corresponding Author: mszydagis@albany.edu

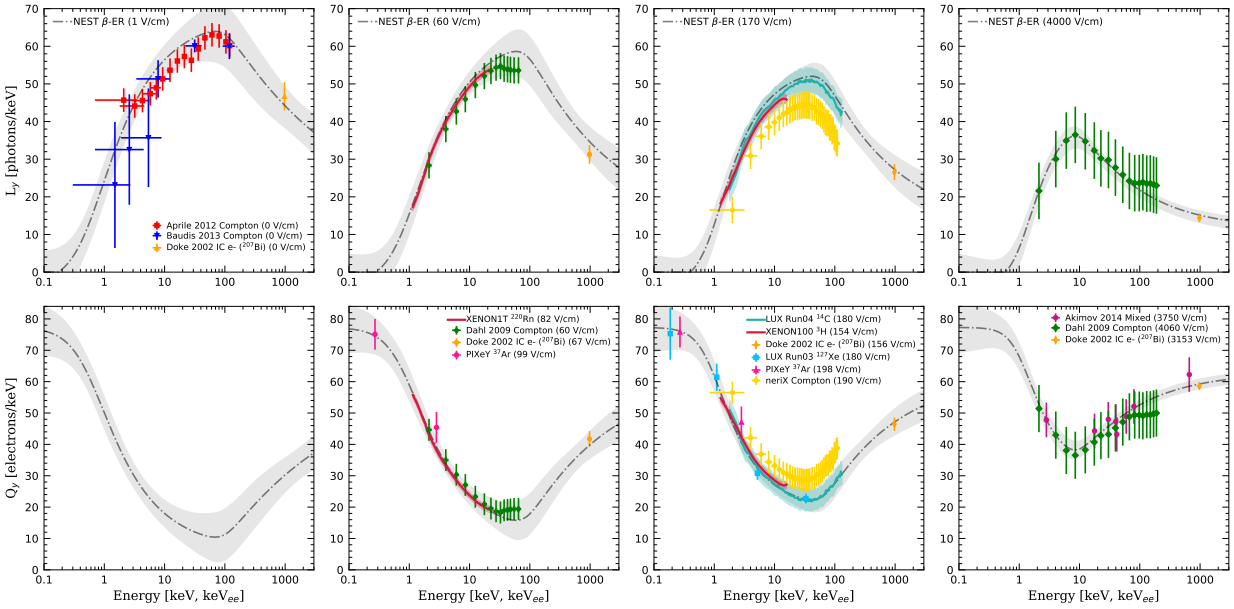

FIG. 1. β electron recoil (ER) L_y (top row) and Q_y (bottom) vs. energy E. Different fields $\mathcal{E}$ are represented, from 0 V/cm at left to the highest fields for which data exist at multiple E's, ∼3-4 kV/cm, at right. More data exist, all of which are utilized to inform NEST, but these are selected as representative examples of the lowest and highest $\mathcal{E}$'s and lowest and highest E, from sub-keV to 1 MeV across different types of experiments [9–19]. Newer results *e.g.* XENON1T's ^{220}Rn calibration illustrate the predictive power of NEST. MC lines are black dashed with gray 1σ error bands, using the latest beta model. It stems from LUX ^{14}C data [15, 20] but was also fit to Compton scatters, which may differ in yields. Evidence for that is modest, and NEST treats them identically. While the main γ model, in the next figure, could be merge-able, it is treated independently at present.

II. SUMMARY OF MICROPHYSICS MODELS

NEST model choices are justified in [21] and in earlier works, but summarized here as a foundation for the main focus. NEST is shared openly, grounded using physically-motivated behaviors for quantum generation from energy deposits, and updated regularly with the latest data [22]. Where possible, relative yields are converted to absolute, if detector gains are calculable. Systematic uncertainties have fallen with increasingly higher-quality calibrations. NEST has been converging on what could be final qualitative shapes for the primary scintillation light (S1) and ionization charge yields (Q or S2, the secondary scintillation) as a function of the energy E, electric field $\mathcal{E}$, and mass density ρ. This is true not only for LXe but also Ar, used by *e.g.* DarkSide and DUNE. These yields differ by particle interaction type, across four orders of magnitude in E. Light yield decreases monotonically as the charge yield increases with increasing drift electric field $\mathcal{E}$ [23].

A. Electronic Recoils (Betas, Gammas, X Rays)

NEST begins with a model of total yield, summing the VUV (vacuum ultraviolet) scintillation photons and ionization electrons produced. IR photons are not included, because the yield in LXe is low [24] and the wavelength is beyond the sensitivity of photon sensors in common use. The work function W_q for production of quanta depends only upon the density, with a simple (linear) fit based on data collected in [25], across solid, liquid, and gas:

$$W_q\ [eV] = 18.7263 - 1.01 \times 10^{-23}\rho_{e^-}. \quad (1)$$

ρ_{e^-} is density in electrons (e^-) per cubic centimeter. LXe TPCs will typically operate at temperatures of 170-180 K and 1.5-2 bar(a) of pressure, leading to a mass density ρ ∼2.9 g/cm^3. This results in a W_q between 13-14 eV [26]. The exciton-ion ratio will determine how generic quanta break down into excited atoms, *i.e.* excitons N_{ex}, versus pairs of ionized atoms with freed electrons N_i:

$$N_{ex}/N_i = (0.067366 + 0.039693\rho) \times \mathrm{erf}(0.05E), \quad (2)$$

where in this case ρ is in g/cm^3, and E is deposited energy in keV, for a beta interaction or Compton scatter. Here the density dependence is based again on [25] while the E dependence comes from reconciling [27–29], given evidence $L_y \to 0$ as E decreases. Ionization electrons can recombine with Xe atoms or escape, given the presence of a drift field. So the number of photons N_{ph} is not simply equal to N_{ex}. This is the source of anti-correlation, motivating the use of both charge and light to measure the energy, $E = W_q\ (N_{ph} + N_{e^-})$ [21]:

$$N_{ph} = N_{ex} + r(E, \mathcal{E}, \rho)N_i \text{ and } N_{e^-} = [1 - r(E, \mathcal{E}, \rho)]N_i, \quad (3)$$

where r is recombination probability for e^--ion pairs. It depends on energy, field, and mass density, as well as particle and interaction type. Experiments most commonly quote results as specific light and charge yields per unit keV, L_y and Q_y, defined as N_{ph}/E and N_{e^-}/E.

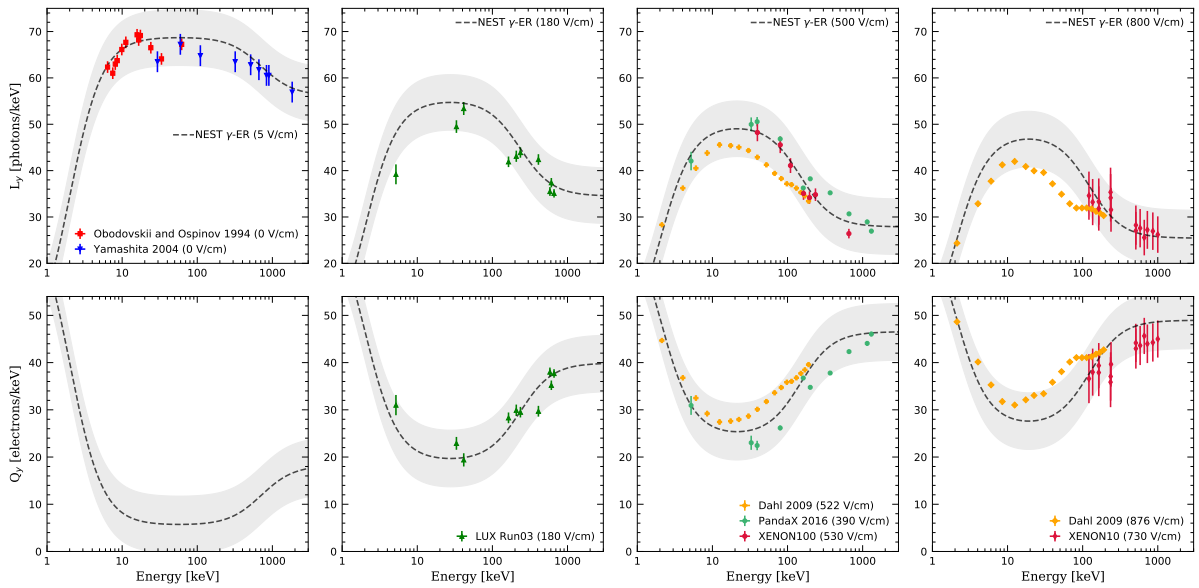

FIG. 2. γ ER L_y (top) and Q_y (bottom) vs. E at $\mathcal{E} = 0$ (left) to nearly 10^3 V/cm (right). Before β calibrations were common, photoabsorption peaks from monoenergetic γ's were used [13, 30–35]. At sufficiently high E, L_y is lower and Q_y higher than in Fig. 1, as some multiple scattering below detector position resolution occurs and is absorbed into NEST: multiple lower-E, higher-dE/dx vertices are "averaged over." Now x is true (γ) E even for data. Low fields again approximate 0 V/cm, when NEST becomes singular. As in other plots gray 1σ bands are driven by data errors, model shape constraints (sigmoidal), and monotonic $\mathcal{E}$ dependence. LUX L_y points but not Q_y seem systematically low due to a different W_q used, with LUX assuming 13.7 eV (no ρ dependence). Dahl data sets exhibit different shapes due to being mixtures of Comptons and photoabsorption.

Q_y is modeled first; L_y is set by W_q and subtraction:

$$N_q \equiv N_{ex} + N_i = N_{ph} + N_{e^-} = E \;/\; W_q, \text{ where}$$
$$N_{e^-} = Q_y E, \text{ and} \quad (4)$$
$$N_{ph} = N_q - N_{e^-}.$$

N_q is the total quanta, and N_{ph} is also $L_y E$. The reason for this procedure is the greater reliability of S2 measurements *cf.* S1 for lower E, as explained in [17, 21]. Q_y in the ER (electron recoil) model is a sum of two sigmoids:

$$Q_y(E,\mathcal{E},\rho) = m_1(\mathcal{E},\rho) + \frac{m_2 - m_1(\mathcal{E},\rho)}{[1+(\frac{E}{m_3})^{m_4}]^{m_9}}$$
$$+ m_5 + \frac{m_6(\equiv 0) - m_5}{[1+(\frac{E}{m_7(\mathcal{E})})^{m_8}]^{m_{10}}}, \quad (5)$$

with m_1 serving as basic, field- / mass-density-dependent level. A fixed m_2 determines low-E behavior, while m_7 controls the field-dependent ($\mathcal{E}$) shape at high E's. These and all m's are empirically determined but the others are constant in $\mathcal{E}$ [20]. (m_6 is defined as exactly zero to avoid degeneracy.) That being said, a combination in NEST of these two specific shapes captures the behavior from two first-principles options – the Thomas-Imel box model at low E [36] and Doke-modified Birks Law at high E [37]. Microphysics above ~15 keV involves cylinder-like tracks. Because of where these E's lie along the Xe Bethe-Bloch curve, dE/dx decreases with increasing E, and, as a result, the recombination probability r and in turn L_y decreases, increasing Q_y [38–40]. Low-E deposits are more amorphous, with straight 1D track lengths becoming ill-defined: r and L_y instead increase with the 3D ionization density and E, as dE/dx instead increases with E.

r is found retroactively in recent NEST versions after fitting to Q_y per Equation (5), chosen to match both the box and Birks models. Using Equation (2) as a constraint avoids degeneracy with N_{ex}/N_i, with the sum $N_{ex} + N_i$ (also equal to $N_{ph} + N_{e^-}$) already constrained by Equation (1) and $N_q = E/W_q$. A raising or a lowering of W_q, an average W, in Equation (4) should change L_y and Q_y equally, preserving both their shapes in E and $\mathcal{E}$ [41].

Figure 1 summarizes both L_y and Q_y from both data and NEST, at $\rho = 2.89$ g/cm^3 ($T = 173$ K, $P = 1.57$ bar) for β interactions, as well as Compton-scatter ER. This is a typical LXe operational point. The non-monotonic E dependence is clear, and decreasing L_y from left to right (top). The Q_y increases (bottom) in anti-correlated fashion as $\mathcal{E}$ increases, suppressing recombination but keeping N_q fixed. The $\mathcal{E}$ dependence is most pronounced at 100-1000 keV, where e^-'s are spread over longer tracks. That may make them more susceptible to drift field. Even at zero field, however, there exists a "phantom" Q_y, as explained in [11, 21]. It is not observable in data, except by noting L_y vs. E is the same shape as at non-zero $\mathcal{E}$. Non-zero fields standing in for 0 represent residual stray fields in a detector and/or the intrinsic fields of Xe atoms [42].

Absorption of any high-E photon, γ or x-ray, is modeled like β interactions and Compton scatters, but with unique m's (Figure 2), to capture sub-resolution multiple scatters and distinct dE/dx. The appendix lists β and γ model parameters, and those for nuclear recoil (NR).

B. Finite Energy Resolution

Energy resolution typically refers to Gaussian widths (σ or FWHM) of monoenergetic peaks from high-E γ-ray photoabsorption, but it is also relevant to lower E's, in WIMP searches. Smearing of continuous ER spectra can drive an increase in signal-like background events. But to understand statistical limitations on high-level parameters like monoenergetic peak σ or background discrimination we must start with lower-level parameters behind all the relevant stochastic processes involved. This modeling is discussed in depth in [21] but portions germane to this work are summarized here.

Realistic smearing of mean yields begins with a Fano-like factor F_q applied to total quanta N_q prior to differentiation into N_{ex} vs. N_i. It is labeled as Fano-like, as it does not follow the strict sub-Poissonian definition [43]. F_q may exceed 1, but is still used in the usual definition of the standard deviation of N_q, namely $\sigma_q = \sqrt{F_q N_q}$.

$$F_q = 0.13 - 0.030\rho - 0.0057\rho^2 + 0.0016\rho^3 + 0.0015\sqrt{N_q}\sqrt{\mathcal{E}} \quad (6)$$

The first line of Equation (6) is a spline of mass-density-dependent data [25] to allow for gas, liquid, or solid. The constant 0.13 represents the theoretical value of the Fano factor in Xe following the traditional definition ($F_q < 1$) and also matches NEXT gas data [44]. The second line of Equation (6) applies only to liquid Xe and is data-driven. The $\sqrt{N_q}$ term is included in order to match the data at MeV scales (*e.g.*, in $0\nu\beta\beta$ searches). Such results did not achieve the theoretical minimum in E resolution even if reconstructing N_q, utilizing both channels of information (light and charge), instead of only a single channel. This was true even for cases where the noise was allegedly subtracted or modeled [45, 46]. The $\sqrt{\mathcal{E}}$ term forces F_q to increase with $\mathcal{E}$. When $\mathcal{E}$ increases, Q_y, already the greater contributor to quanta, increases, causing an improvement in the combined-E resolution. However, it is smaller than naïvely predicted, so the field term decreases the rate at which resolution improves, to match the data [47, 48].

There are many possible explanations for F_q becoming $\gg$1 as E or $\mathcal{E}$ changes. W_q may need to be replaced with separate values for the excitation and ionization processes (both inelastic scattering), then further subdivided into different values that depend upon e^- energy shell. Lastly, elastic scattering of orbital e^-'s may play a role [49].

A Gaussian smearing is applied to N_q having a width σ_q as defined earlier, dependent on F_q; a binomial distribution is then used to divide quanta into excitons and ions in type, following Equation (2).

F_q drives resolution on a combined-E scale, but such a scale is more relevant for monoenergetic peaks than within a WIMP search [13, 21]. The "recombination fluctuations," however, describe variations around the means of Equations (3-5) and are canceled out with combined E. These fluctuations constitute one of the key factors for characterization of discrimination [50]. These are fundamental and do not originate from detector effects [32, 35]. Moreover, they are not binomial, despite recombination (or, escape) appearing to be a binomial choice. Potential explanations for this phenomenon include δ-ray production or other secondary interactions (as observed at different E's in both Ar and Xe [51, 52]), the distinctive statistics of initial (geminate *i.e.* Onsager) recombination with original parent ions as opposed to the volume (columnar) recombination along a track [53], and/or short-lived mesoscale clustering of dimers [54].

While it is unclear which explanation is correct, NEST proceeds with a fully empirical approach to simply model what is observed in data; following [20, 32, 55] closely, NEST defines the variance in the recombination to be:

$$\sigma_r^2 = r(1-r)N_i + \sigma_p^2 N_i^2 \ (\sigma_{e^-} = \sigma_{ph} = \sigma_r), \text{ where}$$
$$\sigma_p = A(\mathcal{E})e^{\frac{-(y-\xi)^2}{2\omega^2}}[1+\text{erf}(\alpha_p\frac{y-\xi}{\omega\sqrt{2}})] \text{ and } y = N_{e^-}/N_q. \quad (7)$$

The $r(1-r)N_i$ in σ_r follows the binomial expectation of $\sigma_r \propto \sqrt{N_i}$. The σ_p term leads to $\sigma_r \propto N_i$, as proposed in [50]. It is a skew Gaussian (on the second line), with an amplitude A depending on $\mathcal{E}$, varying from 0.05-0.1, as needed to simulate the increase in widths of the ER band with higher field [20, 55]. Previously, σ_p was simulated as a constant in NEST similar in value to A, but a constant is inadequate for capturing the full behavior of recombination fluctuations [32].

Instead of σ_p's dependent variable being recombination fraction r it is e^- fraction y, closely related to escape fraction, leading to a better fit to data, and a simpler one, as r cannot be measured directly, only inferred. Recombination probability is degenerate with N_{ex}/N_i, while y is directly measurable. It can be written in terms of r: $y = (1-r)/(1+N_{ex}/N_i)$ [13]. Non-binomial fluctuations decrease as $y \to 1$ or $y \to 0$, as $\sigma_p \to 0$. ξ, ω, and α_p are the centroid, width, and skew of σ_p, respectively. Default NEST values are $\omega = 0.2$, determining the width of σ_p, and $\alpha_p = -0.2$, setting its skewness.

$\xi \approx 0.4 - 0.5$ was found based upon beta and gamma-ray ER data. The types of data utilized were band widths and monoenergetic peak energy resolutions, both at multiple $\mathcal{E}$'s and E's [13, 35, 50]. ξ's value depends on what data sets are used and what other parameters are fixed. ξ is consistent with the most variation occurring at the halfway point in y, as would occur within a regular binomial distribution, wherein r is multiplied by $(1-r)$, as in the first term of σ_r^2 in Equation (7). The asymmetry that stems from the choice of a skew-normal in place of a normal function for σ_p allows for lower y, which occurs at high E's and at low $\mathcal{E}$'s, to exhibit different fluctuations compared to higher y. The latter occurs at low E's and high $\mathcal{E}$'s, *i.e.* greater N_{e^-} and Q_y [20, 50, 56].

The skew Gaussian $\sigma_p(y)$ must not be conflated with the E and $\mathcal{E}$-dependent skew defined by [55]. The latter is not simply a convenient fit for a low-level variable but manifests itself as an asymmetry in the final N_{e^-}, which is generated not from a normal but a skew-normal distribution, of the same form as in Equation (7). The mean

$N_{e^-} = (1-r)N_i$ is smeared using σ_r, but wasn't skewed in earlier NEST iterations. Now, there is the N_{e-} skew α_r, unrelated to α_p, that has a value at typical $\mathcal{E}$'s and WIMP-search E's of $\gtrsim$2. Its origin is not understood.

Later we will see a positive α_r value can lead to better background discrimination than expected for LXe. Weak rejection was expected due to the recombination fluctuations being greater (worse) than binomial, but positive α_r will shift ER events preferentially away from NR (more Q_y). This has already been observed [55].

Lastly, while σ_q leads to correlated change in S1 (L_y) and S2 (Q_y), and σ_r to anti-correlated change, uncorrelated noise also exists, affecting S1 and S2 differently. S1 and S2 gains are understood sources, assuming position-dependent light collection and field non-uniformities are taken into account. Unknown sources are modeled with a Gaussian smearing proportional to the pulse areas [26]. A quadratic term may be necessary at the MeV scale [54]. ER and NR are equally affected by any detector effects (known/unknown). Final E resolutions vs. E are seen for ER and NR in [5, 26] and [5], supplementing validation of means in our Figs. 1-3 with their vetting of fluctuations.

C. Nuclear Recoils (Neutrons and WIMPs)

The number of total quanta for NR, summing charge and light, is modeled as a simple power law. It captures both qualitative and quantitative behaviors of the Lindhard approach to modeling the reduced quanta compared to ER. On the other hand, it also allows for departures from Lindhard at higher E's, lowering the slope of $N_q(E)$ in log space with respect to it. In spite of that flexibility, fewer equations and parameters are involved compared with Lindhard, which is a combination of multiple different power laws inside of a rational function [77].

$$N_q = \alpha E^{\beta}, \text{ where } \alpha = 11^{+2.0}_{-0.5} \text{ and } \beta = 1.1 \pm 0.05 \quad (8)$$

The uncertainties here are one order of magnitude greater than those reported recently for this same power law, as only statistical error was included in Eqn. 6 of [21]. Here, the systematic uncertainties especially in S1 photon detection efficiency and the S2 gain (including electron extraction efficiency) are included, with a data set possessing more points not being over-weighted, nor those from non-monoenergetic sources. In addition, the fit presented here is a result of L_y and Q_y extracted from data as displayed in Figure 3, and directly from S2 vs. S1 "bands."

Equation (8) can be used to define L or quenching factor with respect to ER: $L(E,\rho) = W_q(\rho)N_q(E)/E$. This factor permits one to define the electron equivalent energy in units of keV$_{ee}$ for NR, as L times E in keV$_{nr}$, a best reconstruction of the E of recoiling nuclei on the combined-E scale on average. This L should be applicable to neutrons used for calibrations from various sources, dark matter WIMPs, as well as CEνNS, such as from ^{8}B solar nuclear fusion [7].

The next equation combines N_{ex}/N_i with recombination probability, as their effects are degenerate. While the previous equation set total quanta, this one determines division into the individual yields (charge or light) in an anti-correlated fashion, reducing r with higher $\mathcal{E}$, as the exponent for the drift field is negative.

$$\varsigma(\mathcal{E},\rho) = \gamma\mathcal{E}^{\delta}\left(\frac{\rho}{\rho_0}\right)^{\upsilon}, \quad \text{where } \gamma = 0.0480 \pm 0.0021,$$
$$\delta = -0.0533 \pm 0.0068, \text{ and } \upsilon = 0.3 \quad (9)$$

The reference density $\rho_0 \equiv 2.90$ g/cm^3. The exponent υ for the density dependence is hypothetical. It is not well measured at densities significantly deviating from ρ_0 [13].

We utilize Equation (9) to produce a Q_y equation:

$$Q_y(E,\mathcal{E},\rho) = N_{e^-} \text{ per keV} =$$
$$\frac{1}{\varsigma(\mathcal{E},\rho)(E+\epsilon)^p}\left(1 - \frac{1}{1+(\frac{E}{\zeta})^{\eta}}\right),$$
$$\text{where}$$
$$\epsilon = 12.6^{+3.4}_{-2.9} \text{ keV}, \; p = 0.5,$$
$$\zeta = 0.3 \pm 0.1 \text{ keV}, \text{ and } \eta = 2 \pm 1 \quad (10)$$

Energy deposited is again E (in keV), while epsilon (ϵ), also an energy, is the reshaping parameter for the E dependence. Higher or lower ς lowers or raises the Q_y level respectively, providing the (E-)field dependence. ϵ can be thought of as the characteristic E where the Q_y changes in its behavior from ∼constant at O(1 keV) to falling at O(10 keV). (Note ς has adaptable units of keV^{1-p}.)

ζ and η are the two parameters of the sigmoid that control the roll-off of Q_y at sub-keV energies. They allow for a better match to not only the most recent calibrations [66, 70], but also earlier NEST versions and other past models. Lindhard plus Thomas-Imel has a roll-off, but less steep than data or current NEST [42, 73]. η controls steepness, while ζ represents a characteristic scale for NR removing $1e^-$ [21, 78]. At high E, $p = 0.5$ reproduces $Q_y \propto 1/\sqrt{E}$ (Figure 3).

The total number of photons is derived from the total quanta minus e^-'s. This is the same approach used for ER: the charge yield data are more robust, down to lower E. This subtraction is only a temporary enforcement of the anti-correlation however, as then a second sigmoid, of the same shape as for Q_y but separate, is applied. That permits the NEST model for L_y to be more flexible, in terms of reproducing future data from newer calibrations which could show a drop, or a flattening potentially, due to additional N_{ph} from the Migdal effect [65, 79].

An increase in L_y is possible even as $E \to 0$. It is not unphysical as long as N_{ph} vanishes in that limit.

$$L_y^{'} = \frac{N_q}{E} - Q_y.$$
$$N_{ph} = L_y^{'}E\left(1 - \frac{1}{1+(\frac{E}{\theta})^{\iota}}\right); \; L_y = \frac{N_{ph}}{E},$$
$$\text{where } \theta = 0.3 \pm 0.05 \text{ keV and } \iota = 2 \pm 0.5.$$
$$N_q = N_{ph} + N_{e^-}. \quad (11)$$

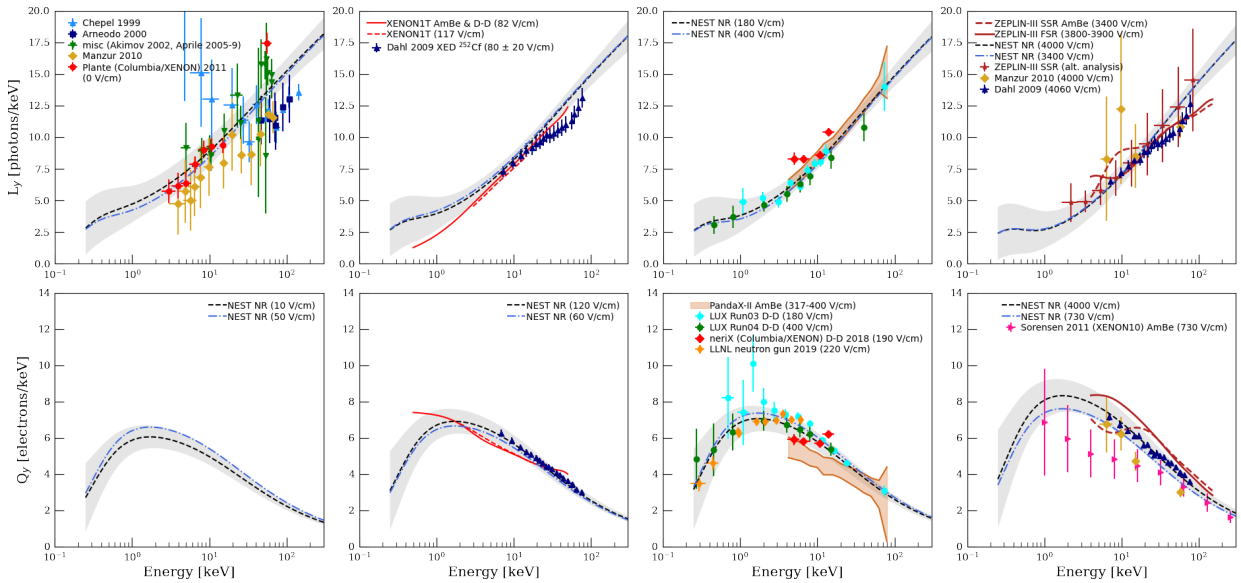

FIG. 3. The NR L_y (top row) and Q_y (bottom row) vs. E at different fields, from 0 V/cm at the left to the highest (E-)fields for which data exist at right, ∼4000 V/cm [6, 12, 13, 57–72]. Newer works from XENON1T and PandaX were not included in fits; there, NEST's predictive power is demonstrated. MC lines are in blue and black. Uncertainties on these increase as E goes to 0 or to infinity, as the amount of data decreases at both extremes. Field dependence is weaker compared to ER. Summing still results in evidence of anti-correlation, just fewer overall quanta [21, 73]. For systematically-offset data sets, our fit can average them if they share the same qualitative trend at least, a sign of a systematic offset in the S1 and/or S2 gains, with the former affected by the 2-PE effect [74] and latter by assuming 100% e^- extraction in early work, prior to recent measurements [75, 76]. Only Chepel 1999 L_y (upper left) is excluded from NEST. As NR dE/dx decreases with decreasing E, e^- escape probability increases, causing L_y to decrease. Its shape is also determined by the L-factor. For Q_y there is a max, as the L-factor decreases and (1-r) increases as $E \to 0$, at different rates. In contrast to [21], where the focus was L, we separate L_y and Q_y here.

$L_y^{'}$ is a temporary variable (perfect anti-correlation) used within NEST to calculate the final L_y and N_q. The best-fit numbers for θ and ι match those of their counterparts ζ and η for Q. In this modular but smooth approach, these sigmoidal terms in L_y and Q_y go to 1.0 with increasing E. In this fashion it is possible to fit the low- and high-E regimes separately, allowing for a possibility that different physics occurs in the sub-keV region, to avoid use of higher-E data to over-constrain lower-E yields.

The two sigmoids lower the predictive power of NEST for extrapolation into newer, lower-E regimes where no calibrations exist. In the case of L_y, it will be challenging to achieve any, at least with reasonable uncertainty. But these NEST formulae are adaptable. The sigmoidal form is also just one minus Birks' Law of scintillation [80] or bi-excitonic quenching [62, 81] as presented.

θ is a physically-motivated characteristic E for release of a single (VUV) photon. Like ζ, its value is 300 eV, in agreement with Sorensen [78] and previous NESTs [42]. Fundamental physics models, such as Lindhard [77] and Hitachi [81, 82] for the L governing total quanta, coupled to the Thomas-Imel "box" model for recombination [36], predict a similar value. Larger θ means more E is needed to produce a single photon (as opposed to excitons) potentially detectable for an experiment, depending upon the light collection efficiency. It means a lower L_y.

$\iota \to 0$ would mean lower L_y as well. For a value of exactly 0, the reduction is a factor of two across all E. On the other hand, in the limit of infinite ι (and/or $\theta \to 0$) the effect of the sigmoid is entirely removed, raising L_y. The same is true for η and ζ in the Q_y formulation. A hard cut-off for any quanta is implemented in NEST for $E < W_q/L \approx 200$ eV. Below that energy, none are generated of either type.

In contrast to ER, the simulated N_q are not varied with a common Fano factor shared by both types of quanta. For NR, there are separate Fano factors for the excitation and ionization, softening the strict anti-correlation at the level of fundamental quanta. $< N_{ex} >$ is smeared using a Gaussian of standard deviation $\sqrt{F_{ex} N_{ex}}$. The $< N_i >$ is similarly varied, with $\sigma = \sqrt{F_i N_i}$ using standard practice for Fano factors [83]. Based on the sparse existing reports of NR energy resolution [65, 70, 84] both F_{ex} and F_i are set to 1.0 in NEST (as of version 2.3.10).

Following Equation (7) from ER: fluctuations in recombination again redistribute photons and electrons prior to the measured S1 and S2.

Parameter values are similar but not identical to those from ER: $A = 0.10$ (fixed for all fields), $\xi = 0.50$, and $\omega = 0.19$ (α_p=0). These set a final recombination width σ_r. N_{e-} and N_{ph} distributions have that width but are also skewed ($\alpha_r = 2.25$), leading to NR band asymmetry. α_r may be higher, but it is difficult to disambiguate NR band skew in data from unresolved multiple scatters or other detector effects [55], or the Migdal Effect [85].

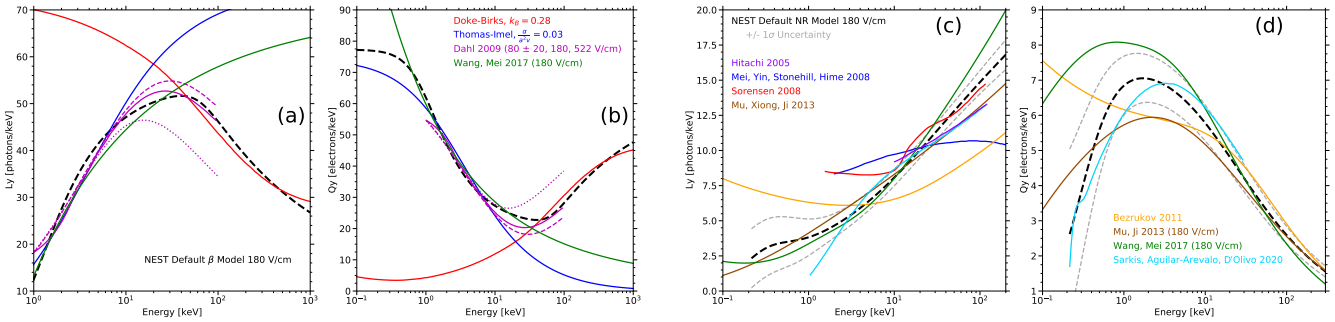

FIG. 4. Comparing NEST to other approaches: L_y (a,c) and Q_y (b,d) alternate, for ER (a,b) and NR (c,d), at 180 V/cm [13, 27, 36, 86]. The second legend applies to both the first and second plots. This was LUX's initial field [87], between XENON1T [88] and earlier works [35]. While similar to fundamental approaches, NEST incorporates features of multiple, splitting differences and following data. Unlike the T-I and plasma models, NEST accounts for high-E (low-dE/dx) L_y decrease (Q_y increase) [86]. Birks does, but fails to work at low E's (high dE/dx) [80]. Dahl presented variations on T-I, usable at high E's by breaking up tracks into boxes, but his closest fields were 80 and 522 V/cm [13]. We show a 180 V/cm model which is a weighted average of the 80 and 522 V/cm models. There are more NR models (at right), due to a need to explain potential WIMPs [81, 86, 89–94]. L_{eff} is relative to ^{57}Co γ-rays (∼122 keV) assuming 64 photons/keV at 0 V/cm with a small error [39, 95] unless papers had a different value. If they presented multiple models, we plot the middle-of-the-road one and/or the one closest to data.

D. Comparisons to First-Principles Approaches

Smoothly interpolating between single-E or single-field data where applicable, NEST is now fully empirical, built on sigmoids and power laws as needed for a continuous model. This causes uncertainty in extrapolating into new E or $\mathcal{E}$ regimes. To address that, we show how the NEST equations follow formulations closer to "first principles." For NEST's earliest version, the Thomas-Imel (T-I) box model [36] was used for low E while for high Birks' Law of scintillation was adopted, in a similar fashion as done by Doke [39], but applied to recombination directly, not just light, so it could work for both light and charge:

$$< r >= \frac{k_A \frac{dE}{dx}}{1 + k_B \frac{dE}{dx}} + k_C, \text{ with } k_C = 1 - k_A/k_B. \quad (12)$$

This is Birks' Law from other scintillators [80], but with a constant accounting for parent-ion recombination [27]. The additional constraint ensures r is between 0-1, as it is a probability. A best fit to ER (γ) data has a non-zero k_C only at zero field; at non-zero $\mathcal{E}$, Equation (12) contains only one free parameter, $k_A = k_B$ (Birks' constant).

The value of Birks' constant at 180 V/cm for LXe appears to be 0.28, if we fit to only the high-E portion of the NEST beta models. Those are in turn supported by data, from LUX and XENON ^{3}H (tritium), ^{14}C, etc. Notably, the value in NEST's first version and first paper ten years ago for this field was 0.257. (See Figure 4.)

Despite the great success of Birks' Law in explaining data at high E's, it cannot capture the behavior of e^-'s or γ's traveling through LXe at ∼ 50 keV and lower E's. While it can be extended by adding higher-order terms in dE/dx, for the lower-E region we turn instead to T-I:

$$< r >= 1 - \frac{\ln(1+\xi')}{\xi'}, \text{ where } \xi' = \frac{N_i}{4} \frac{\alpha'}{a'^2 v_d}. \quad (13)$$

Here, escape probability or $(1 - r)$ for e^-'s in a box was found solving relevant (Jaffé) differential equations [13]. We derive each component of ξ', applying fundamental principles where possible, and other measurements. $\alpha' = De^2/(kT\epsilon_d)$, where D combines the e^- and positive-ion diffusion coefficients, e is the elementary charge, k is Boltzmann's constant, and ϵ_d is the LXe dielectric constant. $D = 18.3$ cm^2/s is the longitudinal diffusion constant for e^-'s in LXe for 180 V/cm, as derived from S2 pulse widths [96]. e^- diffusion dominates over Xe cation diffusion. Assuming this D (and $T = 173$ K as earlier), and $\epsilon_d = 1.85 \times \epsilon_0$, we find $\alpha' = 1.20 \times 10^{-9}$ m^3/s.

We interpret a' ("box size") as corresponding to a ($\mathcal{E}$-independent) e^--ion thermalization distance of 4.6 μm, as calculated by Mozumder [97]. This value was used previously as the border in NEST for track length, to switch from T-I to Birks. Lastly, we assume $v_d = 1.51$ mm/μs at 180 V/cm [98]. The ultimate value of $\alpha'/(a'^2 v_d)$ for that case is 0.0376.

Dahl found best-fit values ranging from 0.03-0.04 for both ER and NR data, between 60-522 V/cm [13]. Our contemporary fits to NEST and to data, the blues lines at low energies in the first two plots at left in Figure 4, used 0.030. If v_d changes with drift field (it is typically O(2 mm/μs) [99]), then the entire ranges of Dahl, and of Sorensen and Dahl, are covered: 0.02-0.05 [73]. Drift velocity can be derived with $v_d = \mu_e(\mathcal{E}) \times \mathcal{E}$. μ_e is e^- mobility. Ignoring the E-field dependence and using its zero-field value [100], but multiplying it by 180 V/cm, one gets 5 mm/μs, the correct order of magnitude at least.

For NR, one sees in Figure 4 right many different past models, mainly for L_y. NEST originally used T-I for NR, as Dahl / Sorensen [13, 73]. See the blue lines in Figure 5. It applies the same color convention as 4. While T-I fixes r, thus partitioning of E into L_y vs. Q_y, total yield must still be determined. For that, we've selected the Lindhard formula, laid out in multiple other works [21, 65, 73, 77].

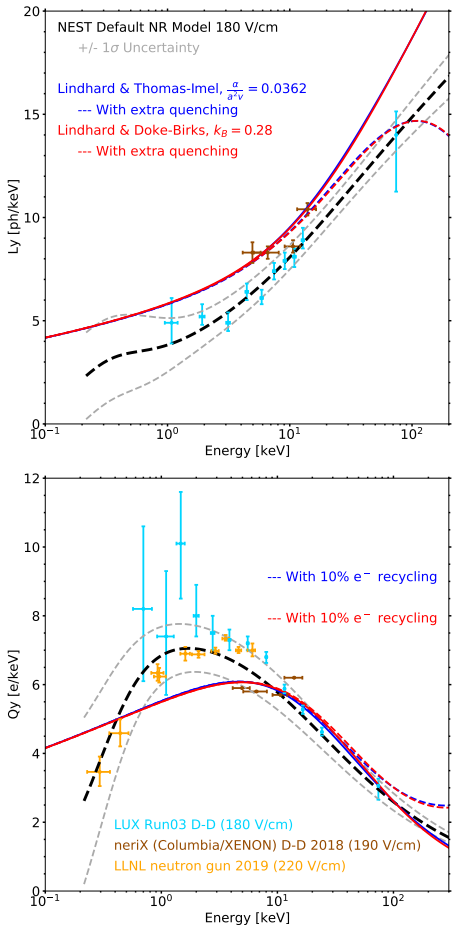

FIG. 5. The comparisons of NEST and select NR data to only the Thomas-Imel (blue) and Birks (red) models for recombination, always using Lindhard for total quanta. For light the dashed lines indicate additional quenching at higher E's and dE/dx, while for charge dashes indicate some "recycling" of photons into e^-'s from that effect (or not, solid). Some data, including at other fields, are consistent at a 1-2σ level with no quenching nor recycling, not the amounts shown here. 50-100 keV$_{nr}$ L_y data are inconsistent: Figure 3 upper left, [63].

We do not allow its effective scaling factor to float, forcing $k_L = 0.166$, the years-old default for xenon [77]. It is also consistent with experimental data [65], the meta-analysis by Lenardo [95], and the latest iteration of NEST.

We identify ς of Equation (10) with $\alpha'/(a'^2 v_d)$, as justified by Equation (9), wherein the parameters for the $\mathcal{E}$ dependence of ς (γ and δ) overlap at the 1σ level with the power-law field dependence of $\alpha'/(a'^2 v_d)$ from an earlier NEST version. At 180 V/cm, $\varsigma = 0.0362$, comparable to ER, and close to our theoretical calculation. We assumed $N_{ex}/N_i = 1.0$, higher than for ER, but the most common assumption for NR, with best fits to actual data as well as theory varying from 0.7-1.1 [73].

An additional quenching is applied to just L_y [62]. We find a common parameterization of this effect [92] to be defined in a manner analagous to Equation (12):

$$q = \frac{1}{1 + \kappa {\epsilon_Z}^{\lambda}}, \text{ with } \epsilon_Z \sim 10^{-3} E, \tag{14}$$

where q reduces N_{ph}. ϵ_Z is called "reduced energy" (unitless), useful for comparison between elements. This equation is similar to (12): the power law can be identified as proportional to NR dE/dx. If we define dE/dx (or LET) as approximately $a\epsilon^{\lambda}$ then $\kappa = k_B a L$. Assuming the ER k_B (0.28 for 180 V/cm), $L \sim 0.15$ (11/73) per Equation (8), and $a = 100$, then $\kappa = 4.20$, $< 0.2\sigma$ away from [95]. N_{ph} "lost" in (14) may be "recycled" into N_{e-}. Figure 5 bottom explores this with a recycle fraction $f_e = 0.1$.

Unlike for ER, Birks can work for NR in place of T-I (Figure 5, red) with $k_B = 0.28$ and $dE/dx = 100\epsilon$. Then $\lambda = 1.0$, possible for NR, though there is disagreement as to whether it is 0.5 or 1.0, depending on E regime [81, 82]. This differs by -1.6σ from a more recent fit [95].

Looking back at alternatives to Lindhard, in Figure 4, we see NEST's unique empirical equations seem to match well with the newest approaches by Mu and Xiong, also Wang and Mei, at least for L_y. NEST's -1σ line touches Sarkis, which is low due to not including the most recent data, such as LUX. On the high L_y end, NEST's upper uncertainty band encompasses neriX [69]. As for the Q_y, it lies between Wang above and Mu and Sarkis below, falling in between the LUX D-D and LLNL data.

We have demonstrated here that despite switching to fully empirical models for maximum flexibility, NEST can model LXe NR and ER well, *i.e.* the most probable dark matter signal and background respectively. This should be true even for regimes where data are still lacking, or exist but have large uncertainties. In the case of NR, we can reproduce all data better with a comparable number of free parameters, but much greater flexibility, compared to semi-empirical approaches. For fluctuations, the number of free parameters increased, to two Fano factors (excitation and ionization) and four numbers for recombination width and skew, to fully capture resolution data.

In the next section, we transition into studying *leakage* of ER into NR phase space, which has multiple axis options. Leakage is defined as 1 or 100% minus discrimination, already explored by *e.g.* LUX [55] and XENON [16], but NEST, justified first by data, is not limited to where data exist to make predictions relevant for a future LXe project. We also attempt to summarize / unify disparate approaches used by experiments currently, weighing advantages / disadvantages of plot aesthetics and ease of analytic fitting. L_y and Q_y will pass through a detector simulation to obtain realistic S1 and S2 pulse areas.

III. KEY APPLICATION: DISCRIMINATION OF BACKGROUND

The discrimination of ER backgrounds from potential NR signals, such as from dark matter WIMPs, requires careful calibrations with radioactive sources first, utilizing betas and gamma rays in the former case, and neutrons in the latter case as representative of WIMPs [101].

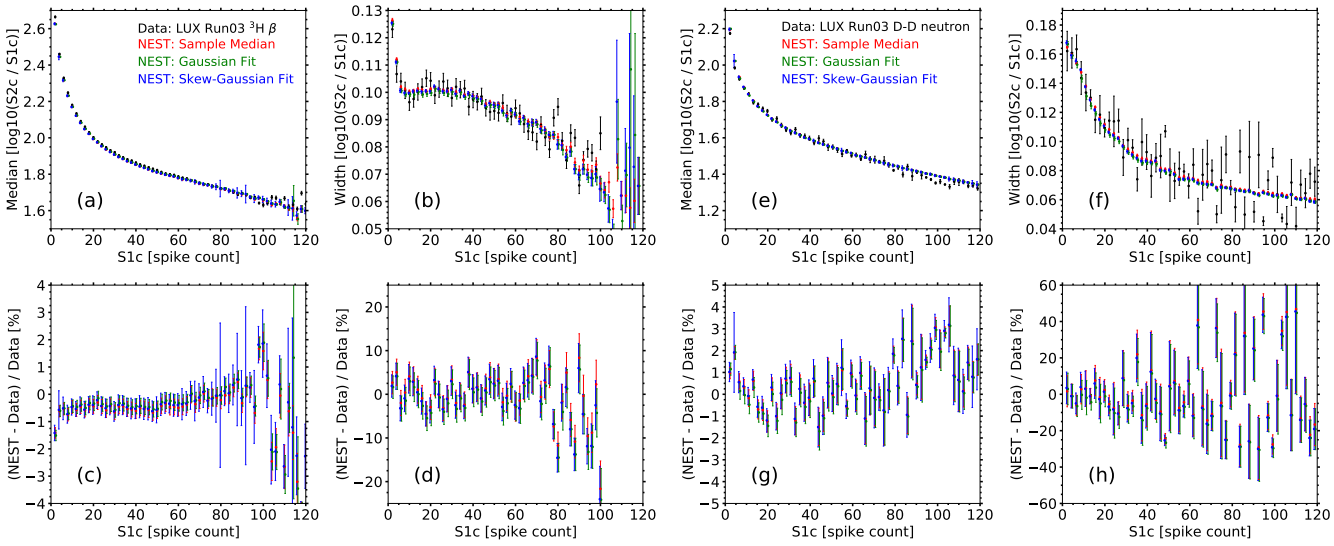

FIG. 6. Decomposition of ER (left plots: a-d) and NR bands (right: e-h) from LUX's first science run, Run03 [98]. ER came from tritium (CH_3T *i.e.* tritiated methane) with a β-decay endpoint of 18.6 keV [28]. NR came from a deuterium-deuterium (D-D) fusion 2.4 MeV neutron gun, leading to Xe recoils up to 74 keV [65]. Plots (a,c,e,g) are concerned with band averages, (b,d,f,h) with widths. The top row is overlays (a,b,e,f), bottom (c,d,g,h) percent differences between NEST and data normalized to data, lined up with the top by mean and width. Different fit styles are indicated in red (raw), green (Gauss), and blue (skew normal) with data in black. Skew fits are best, but endpoints cause statistics to drop at high S1, and such fits are most affected due to the degeneracy caused by adding another free parameter. Percent deviations between model and data are typically an order of magnitude worse for widths compared to means, as they are more challenging to model (second order). But average deviations for S1<100 are typically <1%. S1 units transition from spikes (defined in the text) to phd (photons detected) around 140 due to inability to distinguish individual PMT hits (the number of PMTs was 122). 200,000 ^{3}H (tritium T) and 200,000 D-D events were simulated, roughly matching the number of events in data in the former case, but 10x larger in the latter for easier fitting.

As LXe has been utilized for many decades there are too many experiments to replicate. We thus opted for two examples: 180 V/cm LUX [98], 730 V/cm XENON10 [35]. Together, these address possible E-fields for present and future experiments and photon detection efficiencies. S1 light collection and drift field are leading drivers of ER leakage [16, 50, 55]. Moreover, LUX conducted the greatest number of (original) calibrations [15, 17, 28, 65, 87]. XENON10 was the first LXe TPC for WIMPs [35]. The highest TPC fields achieved, by ZEPLIN-III, were in Figure 3 in the context of NR calibrations, but will also be discussed in this section due to these fields enabling the lowest leakages [102]. Such E-fields may be out of reach in the future due to HV limitations for LXe [103], but they are illuminating for model vetting.

While we cover other possible 2D spaces in Section III C, in Figure 6 we begin with a thorough comparison of NEST to LUX in the traditional parameter space for discrimination. That is the log-ratio of the secondary to the primary scintillation pulse area vs. the primary scintillation signal area [104]. The primary and prompt signal is S1 and the secondary is S2. These are related to the numbers of photons and electrons originally generated, respectively. For S1, there is a position-dependent photon detection efficiency g_1 which is a combination of the geometric light collection with the quantum efficiencies of photo-sensors, like PMTs. g_2 is not an efficiency, and it is >1. It is a gain for e^-'s generating electroluminescence in the gas stage at the top of a 2-phase detector [105]:

$$\text{S1} = N_{ph}\ g_1(x,y,z) \text{ and S2} = N_{e^-}\ e^{\frac{t_d}{\tau_e}}\ g_2(x,y). \quad (15)$$

g_2 depends only upon radial position not the direction of e^- drift (z) in the field. The z-dependence is handled by the exponential correction for e^- lifetime τ_e. Drift time $t_d = \Delta z/v_d$. g_2 is a product of electron extraction efficiency (which depends on extraction field), the number of photons produced per e^-, and the S2 photon detection efficiency (g_1^{gas}) [20]. The number produced per $e-$ depends on gas density, gas gap size, and gas field.

Calibrations enable position corrections for flat-fielding detector response to x=y=0, and to the liquid surface in z for S2s [105]. This results in single values for g_1 and g_2. After correction for internal detector positions, S1 and S2 are sometimes renamed to $S1_c$ and $S2_c$ [20] (alternatively, cS1 and cS2 [88]), but unlabeled S1 and S2 can also mean final corrected values [87, 98]. Published values for LUX's tritium and D-D runs are $g_1 = 0.115 \pm 0.005$ phd/photon and $g_2 = 12.1 \pm 0.9$ phd/e^- [28], and $g_1 = 0.115 \pm 0.004$ and $g_2 = 11.5 \pm 0.9$ [65], respectively. The values needed for good fits in NEST, on both band means and widths, are $g_1 = 0.117$ (both), $g_2 = 12.9$ (tritium), and $g_2 = 12.2$

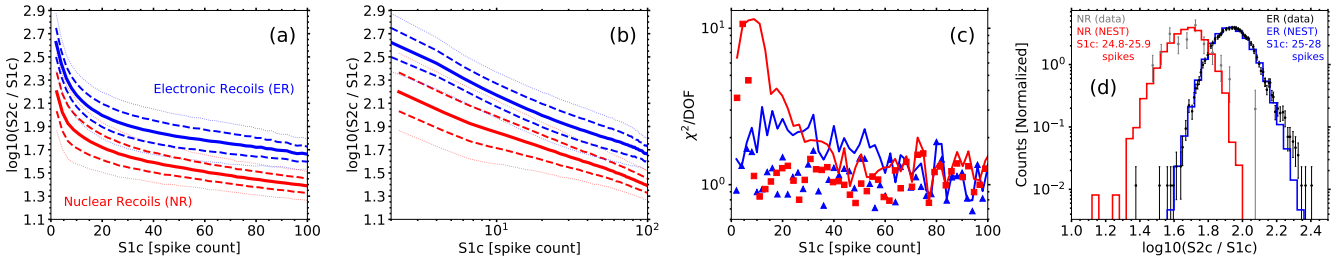

FIG. 7. (a) Band means and widths in one plot illustrate the source of discrimination. ER (blue, ^{3}H) generates more ionization at a given amount of scintillation than NR (red, D-D). Thinner lines, dashed and dotted, represent $\pm$1-2σ on means. (b) The same data shown with a log-x axis better highlights the behavior at the lowest S1s and so lowest E's. These are most important in a dark matter search for a WIMP of any mass, and show how a power-law or log fit is inadequate. Lines in this plot, as in the first, are smooth fits to centroids of fits to histograms for each bin. Those centroids are the individual points shown in Figure 6 top row, the first and third plots (a,e). The fit chosen is an offset hyperbola plus a line, $y' = m'_1/(\mathrm{S1}+m'_2)+m'_3\ \mathrm{S1}+m'_4$. m'_1 and m'_2 are $O(5)$, $m'_3 = O(-0.002)$, and $m'_4 = O(2)$. (c) χ^2/DoF's by bin from comparing data with NEST are in blue for ER, red for NR. Lines represent Gaussian fits, dots skew. NR non-Gaussianity from the combination of single-S1-photon counting systematics with low S2s drives the first three red data points to high values, even for skew fits, which do not capture all non-Gaussianity. This is taken into account in later leakage calculations by considering differing definitions of NR band centroid. (d) Histograms of NEST and data for ER and NR serve as medium-S1 examples. These histograms are not collapsed as in (a,b) on the y axis to means and widths of fits. As they represent different S1 slices [28, 65], NR-ER overlap is worse than it would be at the same S1. These were chosen as the closest S1 bins for which both D-D and tritium histograms were published.

(D-D). These are all well within the uncertainties, with g_2 being the most relevant for setting y-axis levels in Figure 6. The uncertainties as well as the differences in calibration constants between different runs were included in the systematic errors calculated for LUX, as nuisance parameters within the PLR (Profile Likelihood Ratio) null results of its WIMP search [66, 98].

NEST g-values do not match precisely. NEST is not an overfit to the LUX data. It includes results from different global experiments, produced over many decades. Those results were derived from taking S1 and S2 data and solving Equation (15) for N_{ph} and N_{e^-}, to find L_y and Q_y.

The greatest deviations appear for g_2, which had the greatest uncertainty. This was due to the LUX extraction field being below what was necessary to extract close to 100% of drifting e^-'s. While a g_1 is a probability in a binomial distribution, g_2 is more complex, with every step of S2 generation a separate probability distribution [20], as needed to correctly simulate S2 widths.

A. Analytic Fits

Calibration data are commonly binned as in Figure 6. Centroids and widths are reported for each slice in (c)S1; width is not error, typically small for high-stat data, but spread. Skew-Gaussian fits capture non-Gaussianity. In III A and B, when we refer to skew, we mean log(S2) and log(S2/S1) skew, caused directly by what we labelled earlier as α_r (not α_p) and fits capturing that with a skewness parameter. Skew leakage will refer to the leakages calculated using such fits. The possible first-principles origins of skewness at multiple levels are discussed in [21, 26, 55]. Skew fits outperform Gaussian ones (the second plot from the right, Figure 7), always lower in their χ^2 per degree of freedom DoF. The number of degrees of freedom is comparable between non-skew and skew fits, due to a large number of bins, but only one additional free parameter. With the exception of the first couple bins from NR, reduced χ^2's also hover near 1.0, both above and below it, in spite of the increase in the number of free parameters. A fourth, skewness, is added to the three for a Gaussian (amplitude, center, sigma). Asymmetries are clear in the rightmost plot, which shows sample S1 slices. (Note low-E NR has features still not fit well.) The skew fits re-use the functional form of Equation (7)'s second line.

Overall reduced χ^2's are 0.4 (ER band mean), 0.6 (ER width), 1.2 (NR band mean), and 1.1 (width) for binned skew-Gaussian fits, using errors reported by LUX. There are two free parameters in the DoF, the g's, with the linear noise levels set to 0% for S1 and S2. The goodness-of-fit values come from direct comparison with no smoothing to band means or upper/lower uncertainties as done in the first two left plots of Figure 7, which uses an empirical hyperbolic plus linear function explained in the caption. On average the band means and widths differ by $< \pm 1\%$ for both ER and NR, for mean and width alike. The ranges for which these averages as well as the χ^2's are defined are S1=2-99 spikes for ER but 1.7-110.6 for NR. The minima are set by the 2-fold PMT coincidence level, and maxima by the decrease in statistics given the spectral shapes (significantly more events at low E's).

"Spikes" refer to approximately-digital counting of individual photons detected, explained in [98, 108, 109]. Bin widths are 1.0 for ER but 1.1 for NR, where bin centers are not integer values. D-D events were not isotropic in the detector, thus affected differently by position corrections [110]. For each S1 bin (x) the default NEST binning was used in y, of log(S2/S1) = 0.6-3.6 in 30 bins, to cover the extremities out to several sigma. All the other settings were NEST defaults, for the LUX Run03 detector, which comes with a download of NEST (git).

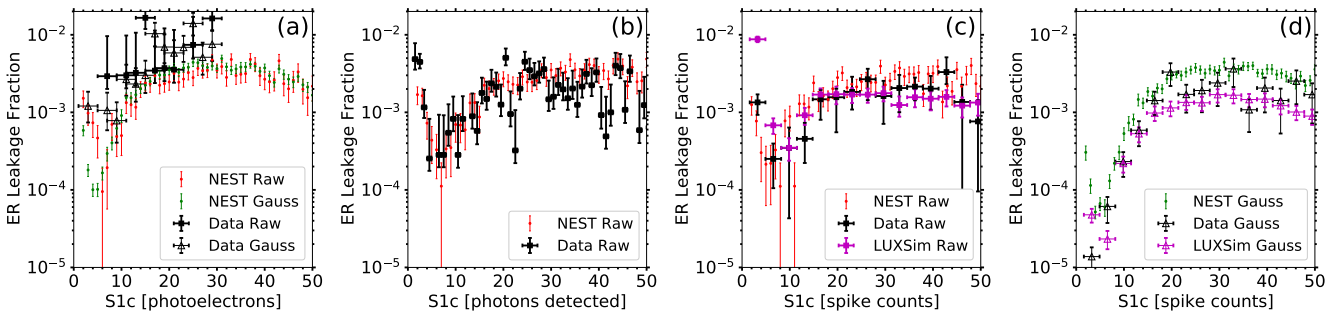

FIG. 8. LUX Run03 tritium and D-D calibration source runs combined to determine ER leakage past the NR band's approximate center line, at 180 V/cm. (a) The first LUX publication [87], which used the traditional units for S1, phe a.k.a. PE. Raw leakage refers to counting the number of ER events which fall below the center of the NR band. Gaussian extrapolations are another option. (b) Later version of the same analysis using the higher-statistics tritium run [28] where the S1 max was also increased, from 30 to 50. The ER yields and backgrounds were better understood out to higher E's. The units were also updated to phd, with (re-)discovery of the 2-phe effect [74]. (c) S1 spike counting, improving upon phd [98, 106]. LUXSim included NEST but also more detail [107]. (d) the same plot as (c) from the same source, but showing Gaussian-defined leakage.

B. Analysis Techniques: Energy Dependence

The fraction of ER events leaking into the NR region in log(S2/S1) vs. S1 space, as defined by Figure 7, is explored as the default quantification of background leakage, not the sole one. We focus first on E dependence, via S1, at one field; the shape is qualitatively similar for all $\mathcal{E}$ [16, 55]. Figures 7-8 indicate leakage can be poor (high) at the lowest S1s, decreases at ∼5-10, increases at 10-20, then flattens. (Later on, we examine how it drops rapidly above S1=50.) These features are driven by variations in the ER and NR band centroids and widths. Low leakage at relatively low S1s, combined with the default WIMP model having an exponential increase in signal at low E's due to the recoil kinematics, make LXe a great medium in the dark matter search. Even though E, and position, resolutions get poorer as E goes to 0, driving the widths of bands higher, the increase in the charge-to-light ratio from ER exceeds NR's. If as was done on LUX, however, the PMT coincidence level is lowered from 3-fold to 2, evidence emerges of leakage degrading again (Figure 8), due to width expansion becoming dominant. Low E's lead to low statistics in N_{ph} and N_{e^-}, thus low pulse areas in S1 and S2, with large relative fluctuations in them.

While a PLR, used in many experimental results now, should account for the overlap of ER with NR in a continuous fashion, as with machine learning techniques [111], a specific and discrete value for the leakage or discrimination is easy to understand and more transparent. It provides rapid comparisons of experimental setups or analysis techniques and enables simple re-analyses of results.

Figure 8 shows leakage vs. S1. In the first plot, a standalone MC tends to underestimate leakage, looking at either raw leakage as measured or Gaussian extrapolation. That was due to NEST not accounting for variation in the 2-phe effect by PMT. In the lowest bins the observed leakage was often 0, leading to empty data bins. Though improvement in leakage through XYZ corrections has already been explicitly demonstrated [112], a phd vs. phe comparison is missing, except across figures from different publications [87, 98]. Figure 8 fills that gap. NEST slightly overestimates leakage between 30-50, but underestimates it in the first few bins, due to not performing a full optical simulation, such as Geant4 [113, 114].

In the third plot, NEST matches well even at low S1s due to spike counting, which removes multiple levels of PMT-specific effects in analysis. LUXSim, based here on an older NEST version, but a more complete MC considering individual PMT effects, overestimates leakage. Low E's are generally hard for MCs. In the fourth plot, still using spikes, Gaussians overestimate leakage at high E but at low underestimate it. The latter led before to the phrase "anomalous leakage" [9]. In this case NEST is not a good fit, but as indicated earlier a Gaussian is not the best fit to ER band slices. But raw leakage is most important. That is what is actually observed, and must be properly modeled, to not overestimate or underestimate backgrounds. LUXSim is a better match here, due not only to optical simulation of each PMT, but LUX-proprietary spike-count code, for data and MC.

While S1 dependence is a good place to start studying leakage given the possible E spectra of potential signals, a single number over an S1 range is helpful. It not only allows for simple comparisons between experiments, but, more importantly, a simpler way to look at another dimension, the field dependence. It also makes it easier to see the non-negligible improvement achieved in moving from S1 as pulse area in photoelectrons to spike counting. That technique reduces the ER band width. The NR width declines as well, but the ER width is more important for leakage, if the NR band mean stays ∼fixed (see Figure 7 left two plots). This is an analysis improvement requiring no alteration in the physical characteristics of a detector, such as higher g_1 and/or drift E-field $\mathcal{E}$.

Skew fits come into play again as another software im-

S1c Range	S1c Units	Counted Leakage $\times 10^{-3}$	Gaussian Leakage $\times 10^{-3}$	Skew Leakage $\times 10^{-3}$
1.5–30	phe, PE	1.69 ± 0.19	2.24 ± 0.16	1.35 ± 0.05
1.5–30	phd	1.74 ± 0.16	2.49 ± 0.71	1.44 ± 0.26
1.5–30	spikes	1.65 ± 0.16	2.28 ± 0.62	1.35 ± 0.25
1.5–50	phe, PE	2.48 ± 0.22	3.24 ± 0.76	2.00 ± 0.30
1.5–50	phd	2.51 ± 0.30	3.31 ± 0.89	2.03 ± 0.37
1.5–50	spikes	2.16 ± 0.24	3.04 ± 0.86	1.77 ± 0.33
1.5–100	phe, PE	2.24 ± 0.16	2.94 ± 0.66	1.78 ± 0.22
1.5–100	phd	2.04 ± 0.04	2.68 ± 0.42	1.67 ± 0.13
1.5–100	spikes	1.69 ± 0.08	2.35 ± 0.35	1.40 ± 0.11

TABLE I. A complete view of mean leakage, across different ranges for S1 (2 to 30, 50, >100), and units for S1: photoelectrons, phd (photons detected), and spikes. The typical NEST errors (systematics from seed choice and binning/fitting algorithms) on these values are 0.3 absolute, or 15% relative. The intermediate stage of phd appears to show worse leakage, but that is due to LUX's detector specifics not being fully modeled. Note that beyond S1= 100 the mean is more stable, due to leakage falling by orders of magnitude (Figure 9).

provement. Table I compares raw, Gauss, and skew leakage, in different S1 ranges. Skew is closer to true leakage (raw *i.e.* counted) measured by counting but has the advantage of functioning when statistics become inadequate for a direct measurement, especially as S1 increases, and spectra of calibrations employed exhibit fall-offs [28, 65]. Skew modeling is applied in NEST not only as fits to individual S1 slices of the ER (and NR) S2 band in data, but directly in recombination: α_r leads to S2 skew.

Skewness modeling and fitting capture both the low-E increase in leakage beyond the naïve Gaussian assumption and high-E decreases in leakage compared to Gaussian fits. Asymmetry in the ER band results in fewer NR-like events. This is beneficial to a WIMP search, as first seen by ZEPLIN at high $\mathcal{E}$ [115]. LUX later re-discovered it at much lower field [55, 66]. Skew may be another way to explain XENON1T's ER tail parameter [116].

Leakage for S1=2-50 spikes is 0.0018, within 1σ of data, even when considering only statistical errors. The most recent LUX analyses concluded 0.0019 ± 0.0002(stat) ± 0.001(syst) [106] (99.81% discrimination). The large systematic error was driven by g_2. It should be the same for ER or NR as a detector property, but may have varied between calibrations. Recall that NEST assigns 12.2 to NR but 12.9 for ER (11.5 and 12.1 in data, each ∼7.5% uncertain). In switching to skew fits, true leakage switches from being 35% overestimated to ∼20% underestimated. These appear to be similar problems, but as we will show next skew fits remain the best choice overall.

Raw and skew are self-consistent for NEST and data, in Figure 9. NEST overestimates the leakage at high S1. Figure 6 (top row, third from left) suggests this is due to NEST's NR band being high. As both the NR L_y and Q_y presented matched D-D data, this is more probably due to the D-D neutron E spectrum and Xe recoil spectrum not being simulated well. These are challenges requiring neutron transport through a complicated geometry [65, 101, 110]. The ER E spectrum is also not a match, a ^{3}H β spectrum, not flat in E [28, 55]. Spectrum is a systematic for leakage (Section III D).

0.005 leakage is neither a mean or a max, as the worst value is 0.004 (or 99.6% discrimination) in Figure 9. The original 99.5% benchmark comes from the completion of XENON10. E-field dependence partially explains it. We know it can be improved on; it has been already.

C. Changing the Discriminant

Discriminant refers in this section to a pair of TPC outputs used for defining (2D) background rejection, the level of which can change with one's choice: historically log(S2/S1) vs. S1, but log(S2) is now more common, fully separating S2 from S1. The band shapes are also simpler (Figure 10 top), as S1 and S2 both increase with the E. Leakage using log(S2) is equivalent: for S1s of up to 100 spikes mean leakage (NEST) is 0.0016 (see the first entry in the last row of Table I). An analytic result with skew fits is also a good match, 0.0015 (last row, third entry). Using Gaussian fits instead again yields an overestimate: 0.00240, similar to the 0.00235 using log(S2/S1). That is only a mean: Figure 10 bottom shows underestimation at low S1s. This is most concerning if that is where most signals may lie. Mean leakages are similar across S1 ranges for different discriminants; we focus on S1<100, due to greater interest in higher E's stemming from EFT [117].

log(S2/S1) vs. S2 [118] exhibits a raw leakage of 0.0043 in LUX Run03. Rejecting S2 in place of S1 as x, another option is E [13]. Combining S1 and S2 has been seen repeatedly to be superior to S1-only E resolution (in some cases S2-only) for ER or NR [21, 23, 54] but that is irrelevant to leakage. The raw leakage for our LUX standard does not improve: 0.0028 (*cf.* 0.002 on LUX, vs. S1 [98]).

For consistency and maximum backwards compatibility of NEST comparisons to the greatest number of older works, we continue with log(S2/S1) as the y axis (S1 as x) for the remainder of this work. Based on this section, our conclusions should be generalizable to log(S2) as y.

Our common x-axis range for each comparison will be S1 = 2–100 spikes (similar to phd) in NEST for LUX's initial WIMP search: 0.0016 raw leakage (or 0.0019 if defined without binning, counting as leakage any ER event with S1<100 falling below a continuous fit to the middle of the NR band) and 0.0015 for skew (*i.e.*, a 99.84-85% discrimination). One built-in feature of NEST is the ability to consider the NR band raw means, medians, or skew/Gaussian-fit centroids (which are not the peak or

mode in skew fits) with or without a continuous fit across S1 bins. This systematic creates a difference far smaller than the 15% error in Table I (see Figure 10 top).

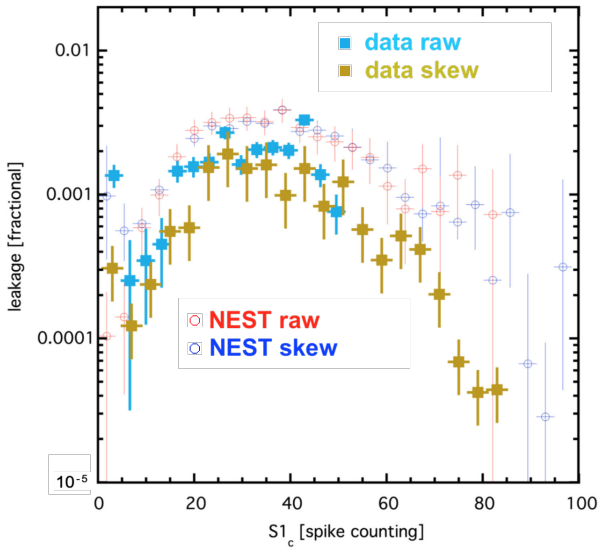

FIG. 9. Leakage in different techniques: raw [106], skew [55]. Offset histogram bin centers and widths are shown for clarity: the latter are 3.35 spikes (cyan squares, identical to Figure 8, second from right), 4 (gold squares), and 3.65 to be in between. NEST is S1=0-98.5 in 27 bins. Red circles are repeated from Figure 8 second from right, but with this different binning, which affects the first few bins the most, thus underscoring the importance of sensible histogram settings when characterizing leakage. NEST's blue circles (skew) match the actual leakage in cyan in the first bin, despite being an analytic approach. They match better than gold, which differs in binning but is the same (actual) data as cyan (light blue).

D. Changing the Underlying Energy Spectra

Contradictory results on leakages from nominally similar experiments may be created by differences in the E spectra of calibration sources. For example, for a similar range of S1s, Dahl [13] found ∼0.004 at 4,060 V/cm, with ZEPLIN-III FSR at 3.85 kV/cm reporting 0.0002 [102]. This would imply leakage isn't universal but depends not only on E range and binning and g_1, but also on the calibration sources, and the exact natures of backgrounds. For ER, interaction type can also change (beta, gamma).

LUX performed only a tritium calibration in its Run03 and ^{14}C β later, with D-D the primary NR calibration, but by establishing NEST agreement with data, we can extrapolate to sources that LUX never deployed, instead of comparing to experiments that used other sources but had different g_1, g_2, $\mathcal{E}$, etc., introducing systematics. Table II has five examples of different ER sources, and five NR. Order of magnitude changes in leakage are possible. Only the raw and skew leakages are reported.

Regardless of what underlying E spectra are assumed, the calculated leakage based on them never exceeds 0.005 in the table. D-D may lead one to conservatively overestimate leakage, compared to AmBe or Cf calibrations, as well as a 50 GeV WIMP. For the bottom half of Table II, there is no more g_2 difference. It is assumed ER and NR must use the same value, and that NEST yields are correct. The D-D run best-fit g_2 was lower, so this conservatively raises the NR band, raising leakage slightly.

Next we study the dependence of leakage on the WIMP

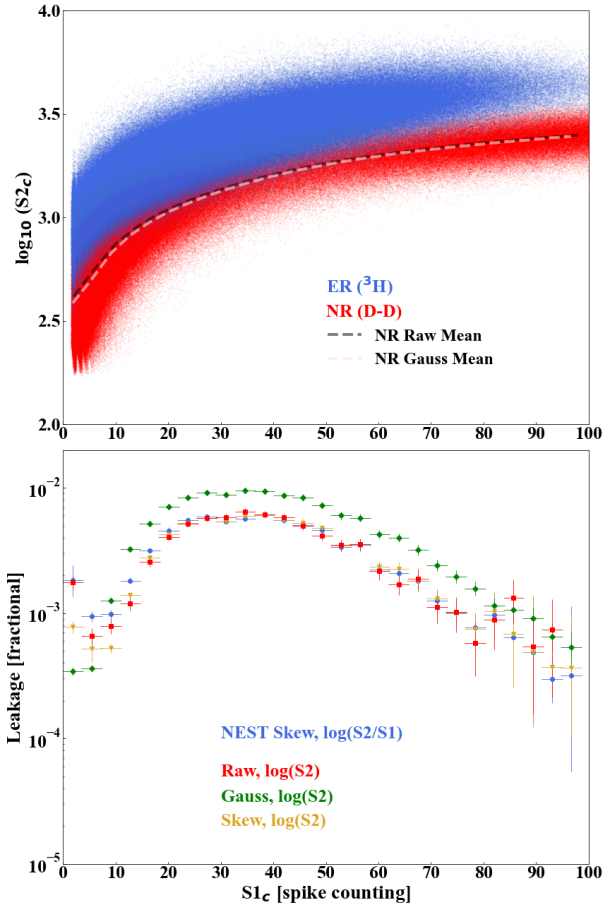

FIG. 10. Top: log(S2) as discriminant in LUX data, as simulated by NEST, for tritium in blue and D-D in red. Discrete points are shown, though the identical functional form from log(S2/S1), a hyperbola plus a line, would fit. This plot highlights different features: higher density in the middle for ER (β spectrum) but at the extremes for NR (D-D E spectrum). At low S1s quantization is evident (from the spike counting). Dashed lines indicate the difference between a line of NR averages and Gaussian centroids. Bottom: log(S2) leakage vs. S1, with NEST skew selected as the example from log(S2/S1) discrimination, repeated from Figure 9 in blue again. Red, green, and yellow are the three options for quantifying leakage, with blue, red, and yellow all consistent across S1s. Green (Gaussians) is the outlier. S2 without a log10 (XENON1T) was not explored as it requires the complication of a log-normal fit or logarithmic bins to work well, in a PLR [119].

mass, showing it improves significantly at lower masses, making LXe a good low-mass DM target. This is the case despite its high mass number, even without considering S2-only analyses [120]. For ^{8}B coherent ν scattering, its E spectrum is most like that of a ∼5-6 GeV WIMP [7].

Source	Raw Leakage	Skew Leakage
Tritium	0.0017	0.0014
^{14}C	0.0010	0.0010
^{220}Rn	0.0012	0.0013
Flat Beta	0.0013	0.0012
ER Mixture	0.0039	0.0035
D-D neutron	0.0025	0.0025
AmBe	0.0019	0.0020
^{252}Cf	0.0018	0.0018
50 GeV WIMP	0.0017	0.0017
Boron-8	$\sim 3 \cdot 10^{-5}$	$\sim 3 \cdot 10^{-5}$

TABLE II. Leakage changing with band shape changing due to E spectrum. All values are NEST's, but vetted using LUX Run03. Top: NR E spectrum is fixed as D-D. The first four rows are different β spectra (^{220}Rn leads to ^{212}Pb [121]). Flat means constancy in E, more representative of a real ER background [26] and lower in leakage [55]. The fifth row is a mix of β or Compton-like interactions with x-ray or gamma-ray photoabsorption: leakage is increased, as Q_y is smaller for gammas [26, 42]. This should not be very applicable to next-gen experiments, where the Rn-chain naked β's and ν interactions will dominate the ER background [122]. This might however explain higher leakage in past ones [104]. Bottom: As a compromise, leakage for the case of a combination of flat beta ER (lowering it) with treatment of the worst-case scenario of the g_2 systematic in LUX (raising leakage more). Maintaining an identical g_2 for ER and NR, the NR sources are: D-D, earlier calibrations, then natural sources.

The source spectrum effect is quantified as a function of WIMP mass in Figure 11. After first matching a real NR band with NEST, the benefit of using ν NR or a WIMP-Xe recoil spectrum to characterize leakage is avoidance of detector geometry specifics, as well as neutron scattering cross-section uncertainties and multiple scattering.

E. WIMP NR Signal Acceptance

Thus far we have used the NR band centroid with linearly or smoothly interpolated (skew-)Gaussian-fit means between S1 bins. This implies 50% signal acceptance for any NR, as assumed for years [35, 104] even with the advent of the PLR, in the latter case as a check [87]. But it is slightly $< 50\%$, due to means and medians differing, as well as fit values compared to raw values. The NR band has positive skew like ER, for multiple reasons, such as recombination and quenching. But, the reduction in acceptance is merely a few percent. Moreover, the opposite effect from negative skew, for different spectra in different detectors, occurs [55, 65, 104].

The leakage for the NR band from a flat-E spectrum under LUX conditions and similarly flat-E β spectrum is 0.00319 raw (0.0032 skew) for 48.7 ± 0.3% acceptance (S1=0-100 spikes). This exceeds the leakage from even a 100 TeV WIMP, the highest mass we tested for Figure 11, with leakage at that high of a mass still only 0.0024 (raw and skew alike). A flat NR band is thus a poor fit even for an ultra-heavy WIMP and should not be used in making projections.

Figure 12 top has different lines for flat-spectrum NR signal acceptance from 5% at the bottom (in red) to 99% at top (in violet). These are still estimates, assuming that Gaussians describe the band slices. Non-Gaussianity may cause a few percent deviation in each bin. The red points, which should be viewed from the right y-axis, break down raw (counting) acceptance by S1 bin, for the black line, which has an overall acceptance in this range of nearly 50% (actual 49%). The low level in the first bin is due to S1 and S2 thresholds removing events from the band.

The middle pane shows leakage as a function of different signal acceptances from the rainbow in the top plot. It demonstrates that even 99.9+% discrimination is possible with reasonable acceptances, of 20-30%. 99.5% discrimination occurs slightly above 50% acceptance.

At bottom is acceptance vs. keV in red (bottom x) and

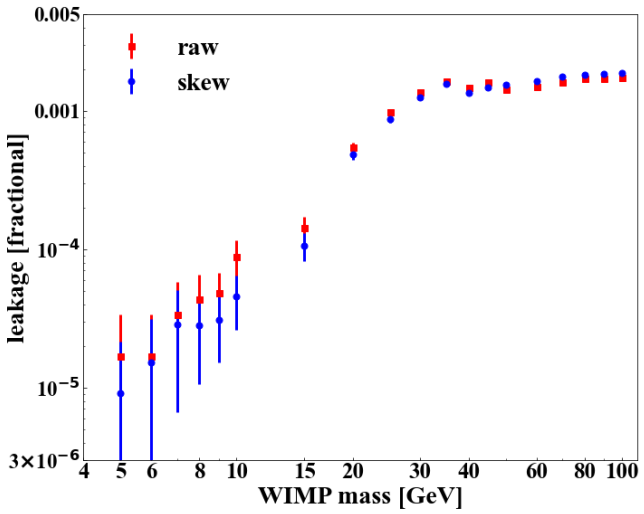

FIG. 11. ER leakage (flat-E background spectrum) as a function of WIMP mass in GeV/c^2 from both counting (red) and skew fits (blue) under LUX Run03 conditions [98]. The former (raw) becomes difficult to quantify, possible only through very long simulation runs (due to the higher statistics required) as mass drops to 0. The leakage asymptotes to a maximum possible value as mass goes to infinity. For clarity, the plot stops at 100 GeV, but masses up to 100 TeV were explored, and the leakage asymptotes to 0.0024 (a 99.77% discrimination), still better than 0.005 (99.50%), despite 180 not being the optimal field for leakage, closer to 300 V/cm [55]. The lower low-mass results, clustered at lower S1s where it was shown leakage rises for a fixed NR band, are due to the NR band centroid moving down in S2, away from ER, as shown in Fig. 7 of [123] for ^{8}B.

mass in GeV in blue (top x) for the case of a traditional, flat band. Not only does the leakage decrease as WIMP mass approaches 0, due to the lower-energy E spectrum, but the acceptance does not correspond with that calculated from a uniform E spectrum. The actual center lines for these lower-E spectra move down in log(S2/S1) away from the ER band. A PLR handles all this internally but these effects are rarely noticed as a result of the "black box" nature of that statistical tool [12, 106].

To capitalize on those effects, experiments will need to address single/few-e^- and photon backgrounds leading to accidentals coincidences, and other effects such as PMT dark noise within detectors with hundreds of PMTs [124]. S1 and S2 thresholds will need to be lowered, especially from 3-fold S1 to 2-fold S1. Recently, this coincidence requirement has instead been increased, due to the larger numbers of PMTs in use, from 2-fold to 3-fold S1. That avoids random noise leading to false-positive S1 signals being reconstructed from individual photo-electrons in a few PMTs [125, 126]. Nevertheless, even for 20 GeV the fraction of WIMP events below a flat NR band mean is already >60%, rising steeply as WIMP mass falls, to over 90% at 5 GeV (consistent with ^{8}B). A PLR will essentially combine enhanced acceptance with lower leakage, by setting an effective acceptance corresponding with an expected leakage of between 0-1 background counts.

F. Switching from LUX to XENON10; Higher S1s

Thus far, the focus has been upon LUX Run03. While this is relevant to LZ's first science run given its comparable conditions [129], this may lead to a narrow view of leakage. So, we consider the dependence of leakage on S1 in XENON10 [35]. It had a lower g_1, but a higher g_2 and fields than LUX, thus making it both similar and different compared to the most recent searches [98, 129]. While it is not likely for future projects to be able to achieve the same field, this is a good second comparison: a non-LUX S1 dependence, at a different (S1) photon detection efficiency ($g_1 = 0.075$ phd/photon $= 0.087$ phe/photon).

In Figure 13 at left, we review distinct interpretations of the same XENON10 data: different S1 ranges, binning, and fit algorithms [35, 127, 128]. The official leakage values are red circles. The middle plot compares NEST with select examples from the left, with the greatest S1 ranges. As seen earlier, Gaussian fits tend to overestimate leakage. However, the raw NEST leakage in this case appears to be an underestimate of the true value. In this case we attempted to duplicate the statistics from the XENON10 calibrations for our comparison, as opposed to the earlier LUX ones, where we instead generated more. That is reflected in the significant NEST (statistical) error bars. While there are some specific systematic disagreements between data and NEST such as raw leakage being too low near S1=10 phe or ∼15 keV$_{nr}$ the agreement is generally good.

The x-axis terminates as high as available at the right

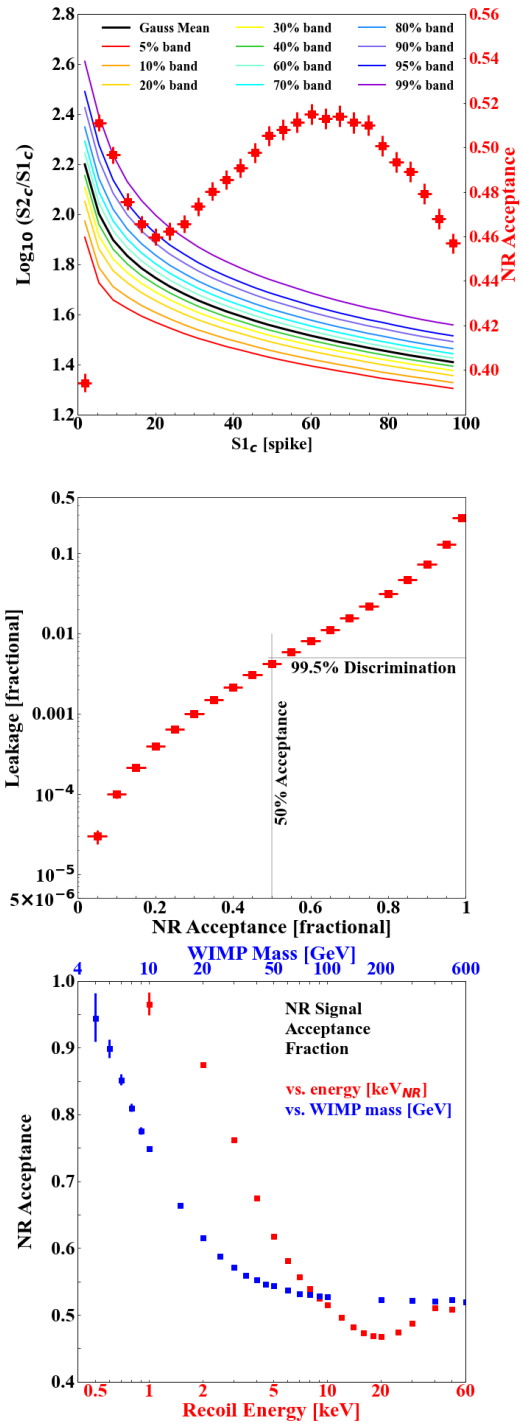

FIG. 12. Top: A color scale of different possible NR band lines of a constant-E spectrum, with 5-99% acceptance underneath. The black line indicates Gaussian means, not medians. 99% is not realistic due to ER, but is included for completeness. The black line is nominally the 50% dividing line. The breakdown of acceptance for S1 bins is in red, exhibiting undulations due to the NR skew changing with E, and averaging to only 49%. Middle: Leakage tied to varying flat signal acceptances at top. Bottom: Signal acceptances as functions of E (not S1) in red and WIMP mass in blue, below the black Gaussian-fit mean, flat-NR line, thus varying in leakage (but always <0.005).

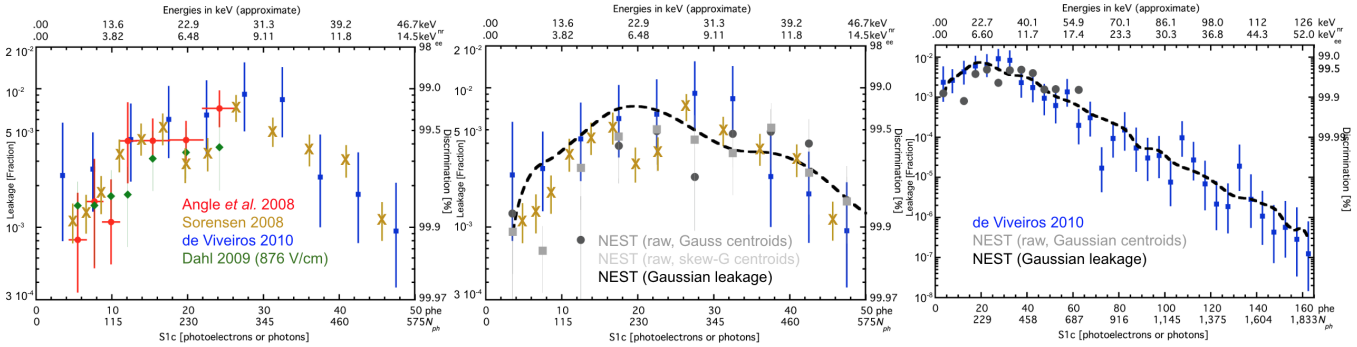

FIG. 13. Left: Different leakage interpretations in the same data: XENON10, 730 V/cm. Red circles [104] and yellow X's [127] are raw, while blue squares [128] and green diamonds [13] are from Gaussian fits, with the latter in another detector (Xed) at a similar field, 876 V/cm. For clarity, x errors, which indicate bin widths, are included only for red, but bin centers/sizes are similar for all points. Only blue and yellow extend beyond XENON10's search window. Bottom x-axes indicate both raw numbers of photoelectrons (XYZ-corrected) as well as a conversion into photons reconstructed using XENON10's $g_1 = 0.075$ [13, 35, 127]. Top axes are approximate central E's for each bin for ER and NR, on an S1-based E scale. Middle: The same yellow and blue points are repeated from the left, omitting others for clarity, while adding the NEST comparisons. Dark gray circles and lighter gray squares are raw leakage in different random instantiations of a simulated XENON10 detector with ER and NR calibration statistics comparable to those in the real experiment. In addition, the darker gray circles use Gaussian fits to determine the NR band centroid, while the light gray squares use skew-Gaussian fits, still using means as a band centroid. They show raw leakages by counting, not extrapolated utilizing the skew functions. In dashed black is a smooth eye-guiding (not a fit) line of Gaussian leakages by bin. Right: The same blue squares and gray circles (errors omitted for clarity) and black dashes from the middle, but extended to high E's. Here NEST is compared to the only available data this high in S1 and E, from a PhD thesis [128].

for XENON10, S1 = 165 phe, still not as high as possible in E, as the NR calibration at the time was AmBe, with an endpoint of 330 keV$_{nr}$. Our plot now ends barely above 100 keV in approximate, reconstructed NR energy (using S1 alone) but these are the highest-S1 data available. No skew fits and/or skew-extrapolated leakage are available for XENON10. We rely upon Gaussian extrapolation for the majority of the bins, above 50-60 keV$_{nr}$, where there are zero counts. NEST agrees well (the blue squares compared to black dashes) concurring on $< 10^{-6}$ leakage above 100 keV$_{nr}$. In a typical SI WIMP search, a LXe TPC cannot capitalize on this, as even large-mass WIMPs produce negligible signal at this high E. However, if one entertains certain EFT operators [117], not only is some signal still possible (as high as 500 keV$_{nr}$), but because of peaks in Bessel-function form factors some operators predict the majority of WIMP signal could occur at hundreds of keV for NR [2, 119]. This has motivated new (D-T) calibrations in this regime [130].

Given the low g_1 and the high E-field, which we will see in the next section is also conservative, the leakages reported in Figure 13 (right) are almost certainly too high. The same NEST models that work for LUX Run04 tritium and ^{14}C data (extending to 156 keV$_{ee}$, *cf.* tritium's 18.6 keV$_{ee}$ max) are used for XENON10. A LAr-like (S1 PSD) leakage [131] is estimated to be achieved of 10^{-9} at S1 = 250 phd. A PICO-like (bubble chamber) level [132] of 10^{-10} appears possible at/above S1 = 300 phd, still only ∼50 keV$_{ee}$ on average for LUX detector conditions, corresponding with only 160 keV$_{nr}$ [66]. With increasing E and S1 (and S2), the ER and NR bands continue to diverge, with ER bands not expanding significantly enough in widths to prevent ER leakage from continuing to decrease (significantly). ^{14}C band data continued in LUX Run04 to its beta endpoint of 156 keV$_{ee}$ at S1s of over 600 phd and corresponding NR energy of 288 keV [15]. In experiments such as LZ [129] and XENONnT [103, 121] ^{220}Rn will serve the same high-E calibration purpose.

There are two important caveats on the benefit of low leakage at higher E's. One is the γ-X *i.e.* MSSI (multiple-scatter, single-ionization) background. It needs to be better understood, via MC, a cut or background subtraction, or a combination. It is doable [119, 133]. The second is gamma photo-absorption peaks exhibiting higher leakage than β's and Compton scatters, due to lower S2s [26].

G. Electric Field and g1 Dependence

XENON10 data at 730 V/cm and the different (lower) g_1 bring us to the question of field dependence, especially on the drift field. XENON10 clearly had poorer discrimination than LUX and other later experiments, despite running at a significantly higher E-field, easier to achieve in the past with lower cathode HV inside a smaller TPC. In its WIMP search space (S1 < 25 phe), the value was 99.6% on average (a 0.004 leakage) and it did drop below 99.5% discrimination (>0.005 leakage) in some S1 bins. See again Figure 13. Part of the solution is: the lower g_1 increased the ER widths, and phe were the S1 units, not phd. (The 2-phe effect was unknown during XENON10.)

Higher $\mathcal{E}$ allegedly improves leakage [136], but thanks to a fuller modeling of the NR and ER band means and ER band widths, there at last exists a more complete an-

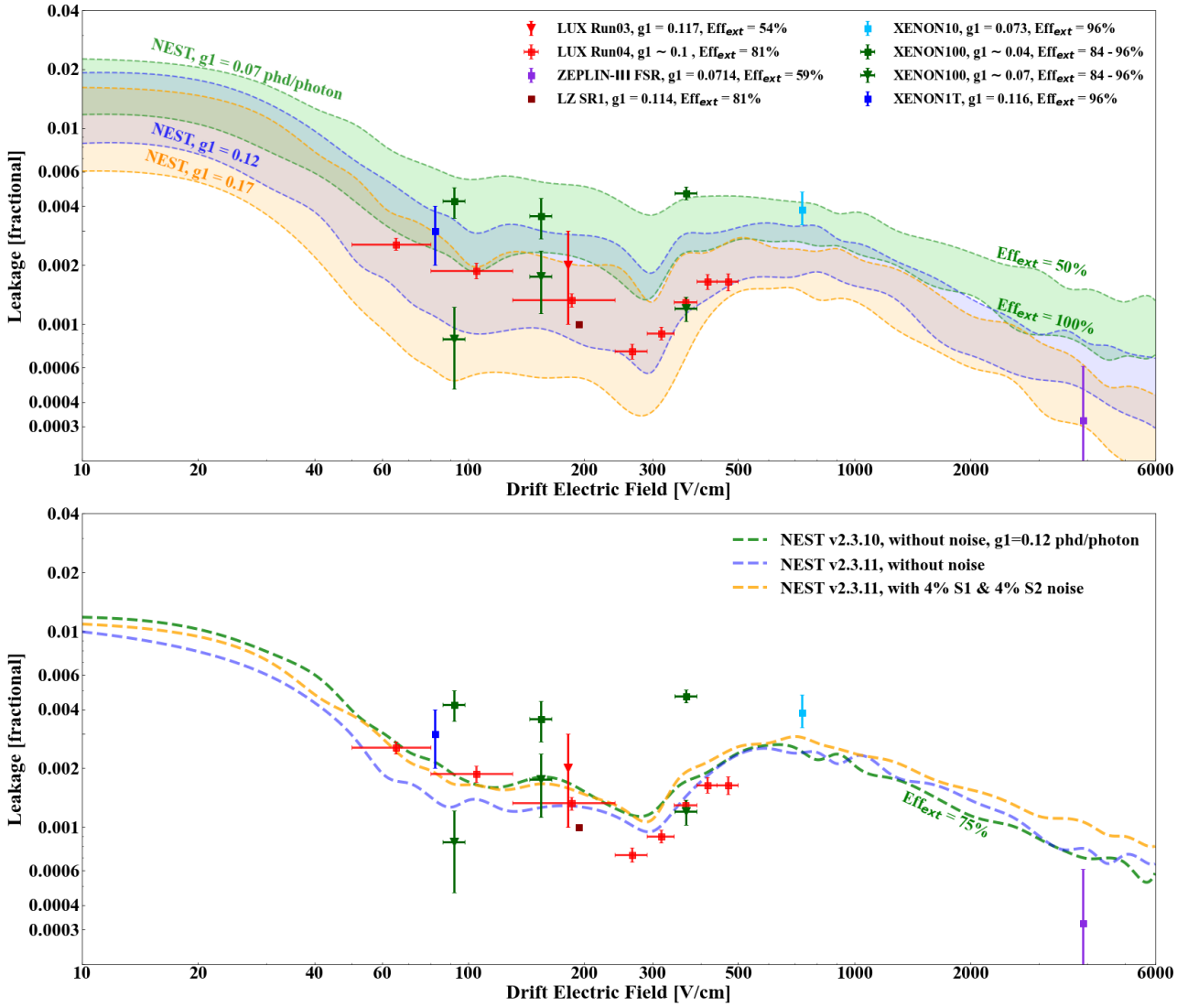

FIG. 14. Top: Summary of known data on ER leakage in LXe [16, 35, 55, 106, 115, 129, 134], for centrally-defined NR bands in log(S2/S1) vs. S1 (colored points with errors) with three NEST examples as colored regions (not fits: smooth eye guides). In the legend, the acronyms FSR and SR1 refer to a first science run. The XENON100 g_1 values were 0.05 and 0.08 PE/photon, where PE is the same as phe (PMT photoelectrons). LZ has no error reported [129]. XENON100 was able to explore different g_1 via detector slices from different positions. Each NEST bands spans 50-100% extraction. The central one uses LUX/LZ/1T-like g_1. The middle of this band should be compared to LUX Run04, with data for the most fields. Data exist for fields not reporting leakage directly, with means and widths still informing NEST between 0-4,000 V/cm. LUX Run03's lower extraction (∼50%) likely causes higher leakage at 180 V/cm, though the (systematic from g_2) error is too large to conclude that. The lowest NEST band is an estimated best possible with current technology, for a moderate-mass WIMP and 50% NR acceptance, combining an LZ-like g_2 [129] with a high g_1, less than the best achieved [135]. The upper (light green) band is close to the lower g_1 value of XENON10, converted into phd/photon. XENON100, which studied $g_1 = 0.07$ plus 0.04, used different E spectra and S1 ranges than the defaults here, so agreement with it is only partial. Bottom: Comparison of NEST version used throughout this work (2.3.10) with the latest one (2.3.11) with ER (and NR) resolution parameters reduced by 10% (and 60) to account for LZ and XENONnT data. Noise is added to raise v2.3.11 in leakage to explain older data. This can be interpreted as earlier iterations of NEST overestimating intrinsic fluctuations, inadvertently absorbing detector effects. That would make this paper conservative.

swer [55]. Fields above $O(1)$ kV/cm will expand the ER band, but pull it farther away from the NR. At E-fields O(100-500) V/cm, there exist undulations in leakage dependence, as the ER band means, NR band means, ER band width, and ER band skewness all change at different rates. We thus have an answer to the origin of the 0.005 leakage benchmark for LXe. The high (730 V/cm) E-field at which XENON10 was able to run accidentally placed it near a local maximum in leakage: see Figure 14. With significantly more data, and an increasing understanding of microphysics modeling, we see that the best field appears to be ∼300 V/cm as an emergent property.

Within uncertainties, there does appear to be a flat region between ∼80-390 V/cm, with contradictory data between XENON100 and LUX Run04, and NEST splitting the difference: Figure 14. This compromise approach for NEST is not forced, as NEST does not, and cannot, (be) fit directly to leakages. Its internal models are based on generating yields and E resolution which match the raw data of ER and NR band means, and widths, from all available calibration data sets, at different fields and g_1.

Neither a PLR nor literal counting of ER background events falling below the NR-centroids curve should exhibit a substantive difference in the final results in this field range. PLR performs background subtraction, while the latter involves a simple, near-50% NR acceptance. Thus, other types of backgrounds may be of greater concern. Nevertheless, a target now exists of 300 V/cm for a next-generation LXe TPC to achieve. Figure 14 suggests that, coupled with a high enough g_1 and g_2 (within reach of current technologies), a similar order of magnitude of leakage and discrimination, $O(10^{-4})$ and 99.99%, can be achieved at that much lower field as at 4 kV/cm.

Lowering NR acceptance, already done on XENON100 [34] and as projected for DARWIN [137], to *e.g.* 25%, has has already been shown in Section E to decrease leakage, so even low fields can lead to competitive searches (limits or discoveries). Achieving a good balance between signal acceptance (NR) and background acceptance (ER leakage) is the same requirement as in any HEP experiment.

Gas field plays a role, too. While the g_1 and drift (liquid) field have the largest impacts, a low extraction efficiency can widen an ER band as low g_1 does. Thus g_1, g_2 (product of single e^- size and extraction), and drift field are all considered together in Figure 14. Within g_2, binomial extraction, a stochastic loss not a fixed reduction, is more important than the precise S2 gain for leakage. A single-phase TPC may resolve this, if it can work well at low, WIMP-search E's (keV scale) not just at the E's of $0\nu\beta\beta$ (MeV) [3, 138].

Earlier the key roles played by the NR and ER E spectra were already addressed, so to maintain simplicity in Figure 14 the NR spectrum was always D-D (based upon the LUX geometry) and the ER one was always flat beta. The latter is an excellent approximation of a full combination of all backgrounds for the WIMP-search-relevant E range in most detectors [26, 129], while the former is approximately like a 50 GeV/c^2 WIMP [65] except with higher leakage (Table II).

As S1 range was also shown to impact leakage, a choice was made for simplicity. Figure 14 shows three S1 search windows, all coupled to a central band for LUX Run04. $g_1 = 0.09$ was tied to an S1 max of 80 phd to follow [55], while the min was determined by the 2-fold PMT coincidence. For the lower band the maximum S1 was extended out to 150 phd, corresponding with the improvement in g_1. For a constant range, distinct g_1's would not show any significant difference in leakage, due to the E range corresponding with the window shifting. Lower-E events will fall below threshold as g_1 decreases, while new, higher-E ones come down into the S1 window. Events at E's with higher and lower probabilities of leakage cancel. For the upper band, S1 = 4.5-20.5 phe in 16 bins, for comparison to XENON10 data (note the change in units) which was also matched earlier, by individual S1 bin.

H. S1 Pulse Shape Discrimination (PSD)

Like LAr's, LXe S1 pulse shape for NR is more prompt compared to ER: dimer singlet states are more likely than triplets. This is due to higher NR dE/dx, and that state having a shorter decay [141]. While PSD can be used in place of log(S2/S1) *e.g.* in a zero-field, single-phase (non-TPC) detector like XMASS previously [142], or in addition [55, 98, 108], it is less effective in Xe. In Ar, the difference in time between the two states is far greater [131]. Nevertheless, our discussion of ER leakage would be incomplete without mentioning PSD.

Pulse shapes were modeled in NEST [140], updated using LUX [108, 111], and checked against XENON [143]. Contradictory data exist on fundamental parameters like singlet/triplet ratio, and the question of a separate (non-zero) recombination time. There are degeneracies across many values, allowing NEST to match contradictory results with one model. *E.g.* an experiment may report no recombination time and more triplets, or higher recombination time and fewer triplets, to produce a similar time profile, even if unlike the singlet and triplet decay profiles the recombination one is non-exponential (t^{-2}) [144].

First-principles aspects of pulse shapes are difficult to model, due to photon travel times (especially in larger detectors) and additional time constants added by PMT internals, cables, pulse-shaping amplifiers, as well as other unique DAQ aspects. Nevertheless, some conclusions are possible from existing work: some degree of PSD exists, but is orders of magnitude lower than LAr's or the S2/S1 discrimination in LXe [141, 142]. But – the combination of PSD with S2/S1 is powerful [55] under specific conditions. The E (and g_1) must be large enough to allow for sufficient photon statistics. This may preclude the vanilla WIMP, but work for a subset of EFT operators, again. Field must also be low enough.

ER and NR S1s become similar as E-field increases in Xe [145]. The one at-scale PSD attempt (WIMP detector) was thus at null field [142]. Singlet/triplet ratio may drop with field [108, 143] and/or recombination time may vanish as it increases. That is reasonable, as recombination is suppressed as S2 increases. At very low E-fields, S1 PSD begins to be usable, if combined with S2/S1, even at traditional WIMP-search energies. That leads to an improvement of more than a factor of 2 outside of error at <100 V/cm and S1 = 10-50 phd [55]. Mid-range S1 also corresponds to the highest S2/S1 leakages (Figure 8). At higher S1s, correlation between NR-like shape and NR-like S2/S1 for ER makes a combination less motivated.

Figure 15 demonstrates the present state of the art. New advances in photo-sensors enabling picosecond tim-

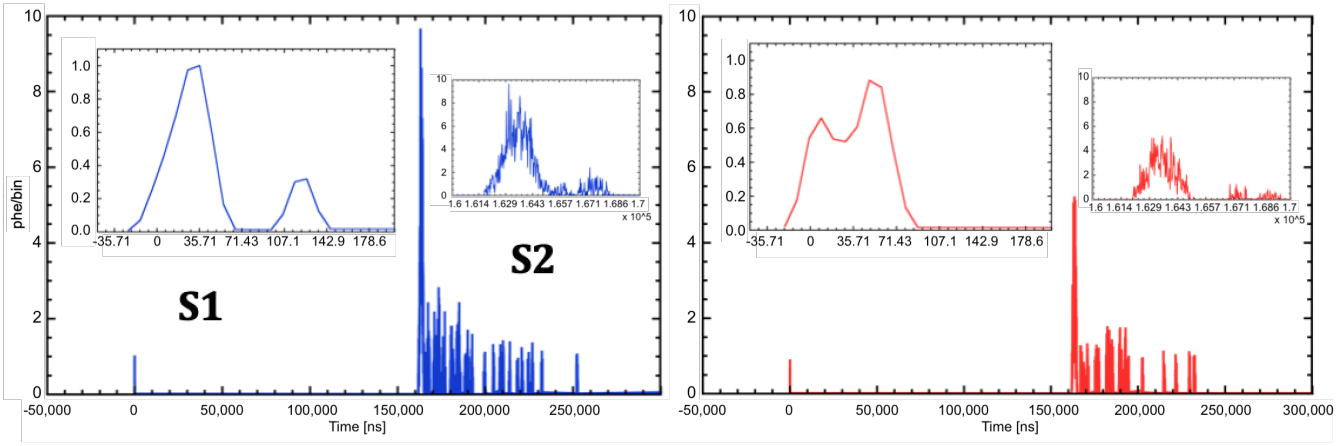

FIG. 15. Sample events demonstrating NEST's S1 and S2 pulse shape simulation capabilities, with ER in blue (2 keV beta) at left and NR in red (8 keV) at right. These are 10 ns time bins, as most experiments employ a 100 MHz digitization rate [125]. Modeling of an e^- train [139] of late-extracted e^-'s is evident as S2 tails. NEST agreement for S1 prompt fraction average and width as functions of E and field is demonstrated in [111] while its agreement on S2 width vs. depth can be found in [140].

ing resolution [146], if they can be leveraged for G3, might make PSD more beneficial. But that is only true if coupled with a sufficiently large g_1. The cylindrical geometry of a TPC (as opposed to spherical like XMASS) may still pose a challenge, due to complicated photon paths from multiple reflections, which reduce the initially ample information from single and triplet decay timing.

IV. DISCUSSION

Starting from models of beta ER, gamma ER, and the NR light and charge yields, along with resolution modeling, a coherent picture was built up within the NEST framework, which enabled a good agreement with data. NEST was also shown to combine features from multiple first-principles approaches like the box and Birks models. As light and charge become the digitized S1 and S2 pulse areas, comparison of NEST to data on means and widths in S2 vs. S1 was next, with LUX Run03 (180 V/cm) as the example detector. LUX also had a very typical photon detection efficiency, $g_1 = 0.117$ phd/photon (S1).

ER backgrounds in the NR regime in S2 vs. S1 were studied as raw leakage or the leakage extrapolated from Gaussian or skew-Gaussian fits. The analytical functions are good for extrapolation in low-statistic calibrations, but neither option is error-free, with Gaussians tending to overestimate leakage and skew-Gaussians underestimating it. The former scenario may be conservative for projecting detector performance, but can lead to artificially-low WIMP limits by an overestimation of expected background in a PLR. The latter (skewed) seems closer to true leakage. As S1 increases, all leakage calculation methods exhibit an increase, then a plateau, followed by a rapid decline as S1 goes to infinity, with increasing energies.

Different S1 units were also probed, starting from basic pulse area in photoelectrons then phd, a unit pioneered by ZEPLIN and LUX, followed by spike units. Pulse areas in phd are lower compared to areas in phe, caused by a statistics-based division of the 2-phe effect, where 1 incoming (VUV) photon can produce multiple phe. Digital counting of individual photons called spike counting is a further improvement, reducing leakage by reducing the ER width. In a PLR any units can be provided: the overlap between the ER and NR populations may remain the same, if the 2-phe effect is measured.

While no significant difference was found between leakage from log(S2/S1) vs. from log(S2), the more common y axis now, the latter has more skew, creating a general overestimate without skew fits, depending on the S1 and the detector conditions. Skew-Gaussian fits perform well in NEST due to its underlying skew-recombination model adding skew to a binomial (Gaussian for high statistics) recombination model for N_{e-}. S2 and E were both worse than S1 as an x axis, for cut and count leakage.

E spectrum makes a major impact on ER leakage as well as NR acceptance, and higher-mass WIMPs will produce higher-E spectra. A softer E spectrum leads to significantly less leakage: ^{8}B (ν) NR and low-mass WIMPs are farther from the ER band. To lower leakage further, NR acceptance can be lowered, to find the optimum balance between acceptance of signal (NR) and the acceptance of background (ER), which are affected by the ER spectrum as well.

The largest leakage, or lowest discrimination, occurred in the first Xe TPC experiment (XENON10) primarily due to the high drift field (in liquid) and can be avoided. Higher g_1 and g_2, the S1 and S2 gains, with higher extraction efficiency through higher gas field in the latter case, can improve leakage, depending on S1 range. Higher liquid field does not monotonically lower leakage. The best field for achieving low leakage at the level of ZEPLIN-III, 2 parts in 10^4, seems to be 300 V/cm, but lower field (50-80 V/cm) may work (<5 in 1000) if coupled to S1-based pulse shape discrimination.

Short-term future work includes a NEST re-writing to account for the lower W_q measured by EXO and Baudis et al. [41, 147]. Secondly, there will be a concerted effort to return to a semi-empirical formulation through applying the modified T-I model pioneered by ArgoNeuT [148], combined with a literal breakup of long tracks into boxes as done in the thesis of Dahl, allowing higher energies to exhibit lower light yields without hard-coding, by virtue of being comprised of multiple, lower-E interactions.

Improved modeling of the MeV scale is important for searches for neutrinoless double-beta ($0\nu\beta\beta$) decay, for which the key discrimination is not NR vs. ER, but between two forms of the latter (β vs. γ). EXO-200 [3] and KamLAND-Zen [149] have produced the two most stringent half-life limits for ^{136}Xe, and are highly competitive with Ge-based experiments. In addition to these results, one must evaluate the prospects of nEXO [150], as well as of LZ [151], XENONnT [152], and XLZD [122] in this field of nuclear physics. The dark-matter-focused experiments have higher background compared to nEXO, but superior energy resolution.

Longer-term future work on NEST will involve molecular dynamics modeling of individual Xe atoms and ions, starting with the 12-6 Lennard-Jones potential of the van der Waals forces. LXe parameters are known, for L-J and for more advanced models [153]. While these approaches are challenging for MeV energies, at sub-keV scales where yields are more uncertain, fewer interactions are involved, leading to a more computationally tractable problem.

ACKNOWLEDGMENTS

This work was supported by the U.S. Department of Energy under Award DE-SC0015535 and by the National Science Foundation under Awards 2046549 and 2112802. We thank the LZ/LUX, plus XENON1T/nT/DARWIN, collaborations for useful recent discussion as well as continued support for NEST work. We especially thank LUX for providing key detector parameters, and LUX collaborator Prof. Rick Gaitskell (Brown University), Dr. Xin Xiang (formerly of Brown, now at Brookhaven National Laboratory), and Dr. Quentin Riffard (Lawrence Berkeley National Laboratory), for critical discussions regarding the detector performance of a potential Generation-3 liquid Xe TPC detector. We also thank Prof. Liang Yang of UC San Diego/nEXO for his support of PhD graduate student Min Zhong.

APPENDIX A: SUMMARY OF NEST MODEL PARAMETERS

In this appendix, we provide tables detailing the functions and model parameters used in NEST for LXe yields from β ER, γ ER, NR, as well as their fluctuations. While NEST has additional models for ^{83m}Kr ER as well as NR from non-Xe nuclei (including α decay), those are not relevant to this work. They can be found in [154].

[1] L. Baudis, European Review (2018), 10.1017/S1062798717000783, arXiv:1801.08128 [astro-ph.CO].
[2] D. S. Akerib *et al.*, Physical Review D **103** (2021), 10.1103/physrevd.103.122005.
[3] G. Anton *et al.* (EXO-200), Phys. Rev. Lett. **123**, 161802 (2019), arXiv:1906.02723 [hep-ex].
[4] E. Aprile *et al.* (XENON1T Collaboration), Nature **568**, 532 (2019), arXiv:1904.11002 [nucl-ex].
[5] D. S. Akerib *et al.*, Astroparticle Physics **125**, 102480 (2021).
[6] B. Yan *et al.*, Chinese Physics C **45**, 075001 (2021).
[7] E. Aprile *et al.*, Physical Review Letters **126** (2021), 10.1103/physrevlett.126.091301.
[8] D. Caratelli *et al.*, "Low-energy physics in neutrino lartpcs," (2022).
[9] E. Aprile, R. Budnik, B. Choi, H. A. Contreras, K.-L. Giboni, L. W. Goetzke, J. E. Koglin, R. F. Lang, K. E. Lim, A. J. Melgarejo Fernandez, R. Persiani, G. Plante, and A. Rizzo, Physical Review D **86** (2012), 10.1103/physrevd.86.112004.
[10] L. Baudis, H. Dujmovic, C. Geis, A. James, A. Kish, A. Manalaysay, T. Marrodan Undagoitia, and M. Schumann, Phys. Rev. D **87**, 115015 (2013), arXiv:1303.6891 [astro-ph.IM].
[11] T. Doke, A. Hitachi, J. Kikuchi, K. Masuda, H. Okada, and E. Shibamura, Japanese Journal of Applied Physics **41**, 1538 (2002).
[12] E. Aprile *et al.* (XENON), Phys. Rev. D **99**, 112009 (2019), arXiv:1902.11297 [physics.ins-det].
[13] C. E. Dahl, *The physics of background discrimination in liquid xenon, and first results from XENON10 in the hunt for WIMP dark matter*, Ph.D. thesis, Princeton University (2009).
[14] E. M. Boulton *et al.*, JINST **12**, P08004 (2017), arXiv:1705.08958 [physics.ins-det].
[15] D. Akerib *et al.* (LUX), Phys. Rev. D **100**, 022002 (2019), arXiv:1903.12372 [physics.ins-det].
[16] E. Aprile *et al.*, Physical Review D **97** (2018), 10.1103/physrevd.97.092007.
[17] D. S. Akerib *et al.*, Physical Review D **96** (2017), 10.1103/physrevd.96.112011.
[18] L. Goetzke, E. Aprile, M. Anthony, G. Plante, and M. Weber, Phys. Rev. D **96**, 103007 (2017), arXiv:1611.10322 [astro-ph.IM].
[19] D. Akimov *et al.*, Journal of Instrumentation **9**, P11014 (2014).
[20] D. S. Akerib *et al.*, Journal of Instrumentation **15**, T02007 (2020).
[21] M. Szydagis, G. A. Block, C. Farquhar, A. J. Flesher, E. S. Kozlova, C. Levy, E. A. Mangus, M. Mooney, J. Mueller, G. R. C. Rischbieter, and A. K. Schwartz, Instruments **5** (2021), 10.3390/instruments5010013.
[22] M. Szydagis *et al.*, "NEST: Noble Element Simulation Technique, A Symphony of Scintillation," (2020).

TABLE III. Table of NEST model parameters comprising the β ER yield models for total light and charge shown in Equation (5).

m_1	Stitching-region yield for β ER charge yields between low and high energies, depending on field and density: $m_1 = 30.66 + (6.20 - 30.66)/(1 + (\mathcal{E}/73.86)^{2.03})^{0.42}$ at a typical LXe density. Takes values $\mathcal{O}(10$ keV$^{-1})$ for $\mathcal{O}(100$ V/cm) fields.
m_2	Low-energy asymptote of the β ER charge yield equation. Default value is approximately 77.3 keV^{-1}.
m_3	Controls the energy-dependent shape of the β charge yields in the low-energy (Thomas-Imel) regime: $m_3 = \log_{10}(\mathcal{E}) \cdot 0.14 + 0.53$. Field-dependent function, with values of approximately 0.8-1.5 keV for $\mathcal{O}(100$ V/cm) fields.
m_4	Field-dependent control on the energy-dependent shape of the β charge yields at lower energies: $m_4 = 1.82 + (2.83 - 1.82)/(1 + (\mathcal{E}/144.65)^{-2.81})$. Takes values from approximately 2.0-2.8 for $\mathcal{O}(100$ V/cm) fields.
m_5	High-energy asymptote of the β charge yield model. Defined as: $m_5 = \frac{1}{W} \cdot [1 + N_{ex}/N_i]^{-1} - m_1$ (See Ref. [20].)
m_6	Low-energy asymptote of the higher-energy behavior for β ER charge yields. Degenerate with m_1 and explicitly set to 0 keV^{-1}.
m_7	Field-dependent scaling on the behavior of the β charge yields at higher energies: $m_7 = 7.03 + (98.28 - 7.03)/(1. + (\mathcal{E}/256.48)^{1.29})$. Takes values $\mathcal{O}(10$ keV) for $\mathcal{O}(100$ V/cm) fields.
m_8	Control on the energy-dependent shape of the β charge yields at higher energies. The default value is a constant, 4.3.
m_9	Asymmetry control on the low-energy behavior. The default value is a constant, 0.3.
m_{10}	Asymmetry control on the high-energy behavior of the β charge yields model: $m_{10} = 0.05 + (0.12 - 0.05)/(1 + (\mathcal{E}/139.26)^{-0.66})$. Field-dependent function that takes values $\sim$0.1 for $\mathcal{O}(100$ V/cm) fields.

TABLE IV. Table of NEST model parameters comprising the γ ER yield models for total light and charge shown in Equation (5). The parameters go into the same functions as those for β ER yields in the previous table.

m_1	Field-dependent function controlling the transition between lower and higher energies: $m_1 = 34.0 + (3.3 - 34.0)/(1 + (\mathcal{E}/165.3)^{0.7})$.
m_2	Low-energy asymptote of the γ ER charge yield equation, defined as $1/W_q$ in units of keV^{-1}.
m_3	Controls the energy-dependent shape of the γ charge yields in the low-energy (Thomas-Imel) regime; a constant value of 2 keV is used.
m_4	Control on the energy-dependent shape of the γ charge yields at lower energies; a constant power of 2 is used.
m_5	High-energy asymptote of the γ charge yield model. Defined as: $m_5 = 23.2 + (10.7 - 23.1)/(1 + (\mathcal{E}/34.2)^{0.9})$.
m_6	Low-energy asymptote of the higher-energy behavior for γ ER charge yields. Degenerate with m_1 and explicitly set to 0 keV^{-1}.
m_7	Field-dependent and density-dependent scaling on the behavior of the γ charge yields at higher energies: $m_7 = 66.8 + (829.3 - 66.8)/(1 + (\rho^{8.2} \cdot \mathcal{E}/(2.4 \cdot 10^5))^{0.8})$.
m_8	Control on the energy-dependent shape of the γ charge yields at higher energies. Default value is a constant power of 2.
m_9	Asymmetry control on the low-energy behavior: unused for γ ER yields and set to unity.
m_{10}	Asymmetry control on the high-energy behavior of the γ charge yields model: unused for γ ER yields and set to unity.

TABLE V. Table of NEST model parameters comprising the NR mean yield models for total light and charge shown in Equations (10) and (11).

α	Scaling on NR total quanta. Default value is $11^{+2.0}_{-0.5}$ keV$^{-\beta}$.
β	Power-law exponent for the NR total quanta. Default value is 1.1 $\pm$ 0.05.
ς	Field dependence in NR light and charge yields, with mass-density-dependent scaling (Equation (9)).
ρ_0	Reference density for scaling density-dependent NEST functions: 2.9 g/cm^3.
v	Hypothetical exponential control on density dependence in ς; the default value is 0.3.
δ	Power-law exponent in the field dependence in ς; default value is -0.0533 $\pm$ 0.0068.
γ	Power-law base for the field dependence in ς. Default value is 0.0480 $\pm$ 0.0021.
ϵ	Reshaping parameter for NR charge yields, controlling the effective energy scale at which the charge yield behavior changes. The default value is $12.6^{+3.4}_{-2.9}$ keV.
p	Exponent which controls the shape of the energy dependence of the NR charge yields at energies greater than $\mathcal{O}(\epsilon)$. Default value is 0.5.
ζ	Controls the energy dependence of the NR charge yields roll-off at low energies. Default value is 0.3 $\pm$ 0.1 keV.
η	Controls energy-dependent shape of the NR charge yields roll-off at low energies. Default value is 2 $\pm$ 1.
θ	Controls the energy dependence of the NR light yields roll-off. Default value is 0.30 $\pm$ 0.05 keV.
ι	Controls the shape of the energy dependence of the NR light yields roll-off. Default value is 2.0 $\pm$ 0.5.

TABLE VI. Table of NEST model parameters for different types of fluctuations for ERs and NRs.

F_q	Fano-like factor for statistical fluctuations. For ERs, this is proportional to $\sqrt{E \cdot \mathcal{E}}$; see Equation (6). For NRs, this is separated into fluctuations for N_{ex} and N_i; the default value is 0.4 for both in NEST v2.3.11, while the values were 1.0 in previous NEST versions.
σ_p	Non-binomial contribution to recombination fluctuations, modeled as a skew Gaussian in electron fraction space.
A	Amplitude of non-binomial recombination skew Gaussian. For NRs, this is a constant 0.04 (v2.3.11) or 0.1 (v2.3.10). For ERs, it is field-dependent: $A = 0.09 + (0.05 - 0.09)/(1 + (\mathcal{E}/295.2)^{251.6})^{0.007})$, where 0.05 was 0.055 in 2.3.10
ξ	Centroid-location parameter of the non-binomial recombination skew Gaussian. Default value for ERs is an electron fraction of 0.45, but 0.5 for NRs.
ω	Width parameter for the non-binomial recombination skew Gaussian. Takes value of 0.205 for ERs and 0.19 for NRs.
α_p	Skewness parameters for the non-binomial recombination skew Gaussian. Takes the value -0.2 for ERs, while being zero for NRs.
α_r	Additional skewness within the recombination process itself. Field- and energy- dependent equations can be found in Ref. [55] for ERs, while it is fixed at 2.25 for NRs, with evidence of higher values in [55]

[23] E. Conti *et al.*, Physical Review B **68** (2003), 10.1103/physrevb.68.054201.

[24] G. Bressi, G. Carugno, E. Conti, C. Noce, and D. Iannuzzi, Nuclear Instruments and Methods in Physics Research Section A: Accelerators, Spectrometers, Detectors and Associated Equipment **461**, 378 (2001), 8th Pisa Meeting on Advanced Detectors.

[25] E. Aprile, A. E. Bolotnikov, A. I. Bolozdynya, and T. Doke, "Noble Fluids as Detector Media," in *Noble Gas Detectors* (John Wiley & Sons, Ltd, 2006) pp. 16–17.

[26] M. Szydagis, C. Levy, G. Blockinger, A. Kamaha, N. Parveen, and G. Rischbieter, Phys. Rev. D **103**, 012002 (2021), arXiv:2007.00528 [hep-ex].

[27] T. Doke, A. Hitachi, J. Kikuchi, K. Masuda, H. Okada, and E. Shibamura, Japanese Journal of Applied Physics **41**, 1538 (2002).

[28] D. S. Akerib *et al.*, Phys. Rev. D **93**, 072009 (2016).

[29] Q. Lin, J. Fei, F. Gao, J. Hu, Y. Wei, X. Xiao, H. Wang, and K. Ni, Phys. Rev. D **92**, 032005 (2015), arXiv:1505.00517 [physics.ins-det].

[30] I. Obodovskii and K. Ospanov, Instruments and Experimental Techniques **37**, 42 (1994).

[31] M. Yamashita, T. Doke, K. Kawasaki, J. Kikuchi, and S. Suzuki, Nuclear Instruments and Methods in Physics Research Section A: Accelerators, Spectrometers, Detectors and Associated Equipment **535**, 692 (2004).

[32] D. S. Akerib *et al.*, Physical Review D **95** (2017), 10.1103/physrevd.95.012008.

[33] A. Tan *et al.* (PandaX-II Collaboration), Phys. Rev. Lett. **117**, 121303 (2016).

[34] E. Aprile *et al.* (XENON100 Collaboration), Phys. Rev. Lett. **105**, 131302 (2010).

[35] E. Aprile *et al.*, Astroparticle Physics **34**, 679 (2011).

[36] J. Thomas and D. A. Imel, Phys. Rev. A **36**, 614 (1987).

[37] T. Doke, H. J. Crawford, A. Hitachi, J. Kikuchi, P. J. Lindstrom, K. Masuda, E. Shibamura, and T. Takahashi, Nuclear Instruments and Methods in Physics Research Section A: Accelerators, Spectrometers, Detectors and Associated Equipment **269** (1988), 10.1016/0168-9002(88)90892-3.

[38] M. Szydagis *et al.*, "Noble element simulation technique," (2022).

[39] M. Szydagis, N. Barry, K. Kazkaz, J. Mock, D. Stolp, M. Sweany, M. Tripathi, S. Uvarov, N. Walsh, and M. Woods, JINST **6**, P10002 (2011), arXiv:1106.1613 [physics.ins-det].

[40] M. Berger, J. Coursey, M. Zucker, and J. Chang, "ESTAR, PSTAR, and ASTAR: Computer Programs for Calculating Stopping-Power and Range Tables for Electrons, Protons, and Helium Ions," (National Institute of Standards and Technology, Gaithersburg, MD 2005).

[41] G. Anton *et al.* (EXO-200), Phys. Rev. C **101**, 065501 (2020), arXiv:1908.04128 [physics.ins-det].

[42] M. Szydagis, A. Fyhrie, D. Thorngren, and M. Tripathi, JINST **8**, C10003 (2013), arXiv:1307.6601 [physics.ins-det].

[43] T. Doke, A. Hitachi, S. Kubota, A. Nakamoto, and T. Takahashi, Nuclear Instruments and Methods **134**, 353 (1976).

[44] V. Alvarez *et al.* (NEXT), Nucl. Instrum. Meth. A **708**, 101 (2013), arXiv:1211.4474 [physics.ins-det].

[45] S. Delaquis *et al.*, Journal of Instrumentation **13**, P08023 (2018).

[46] E. Aprile *et al.*, The European Physical Journal C **80** (2020), 10.1140/epjc/s10052-020-8284-0.

[47] E. Aprile, K. L. Giboni, P. Majewski, K. Ni, and M. Yamashita, Physical Review B **76** (2007), 10.1103/physrevb.76.014115.

[48] E. Aprile, R. Mukherjee, and M. Suzuki, Nuclear Instruments and Methods in Physics Research Section A: Accelerators, Spectrometers, Detectors and Associated Equipment **302**, 177 (1991).

[49] R. L. Platzman, International Journal of Applied Radiation and Isotopes **10**, 116 (1961).

[50] A. Dobi, *Measurement of the Electron Recoil Band of the LUX Dark Matter Detector With a Tritium Calibration Source*, Ph.D. thesis, Maryland U., College Park (2014).

[51] S. Amoruso *et al.*, Nuclear Instruments and Methods in Physics Research Section A: Accelerators, Spectrometers, Detectors and Associated Equipment **523**, 275 (2004).

[52] J. Thomas, D. A. Imel, and S. Biller, Phys. Rev. A **38**, 5793 (1988).

[53] D. R. Nygren, Journal of Physics: Conference Series **460**, 012006 (2013).

[54] C. Davis *et al.* (EXO-200), JINST **11**, P07015 (2016), arXiv:1605.06552 [physics.ins-det].

[55] D. S. Akerib *et al.*, Physical Review D **102** (2020), 10.1103/physrevd.102.112002.

[56] G. R. C. Rischbieter, *Signal Yields and Detector Modeling in Xenon Time Projection Chambers, and Results of an Effective Field Theory Dark Matter Search Using LUX Data*, Ph.D. thesis, UAlbany SUNY (2022).

[57] V. Y. Chepel *et al.*, Proceedings of the 1999 IEEE 13th International Conference on Dielectric Liquids , 52 (1999).

[58] F. Arneodo *et al.*, Nucl. Inst. and Meth. A **449**, 147 (2000).

[59] D. Akimov *et al.*, Phys. Lett. B **524**, 245 (2002).

[60] E. Aprile *et al.*, Phys. Rev. D **72**, 072006 (2005).

[61] E. Aprile, L. Baudis, B. Choi, K. L. Giboni, K. Lim, A. Manalaysay, M. E. Monzani, G. Plante, R. Santorelli, and M. Yamashita, Physical Review C **79** (2009), 10.1103/physrevc.79.045807.

[62] A. Manzur, A. Curioni, L. Kastens, D. McKinsey, K. Ni, and T. Wongjirad, Phys. Rev. C **81**, 025808 (2010), arXiv:0909.1063 [physics.ins-det].

[63] G. Plante *et al.*, Phys. Rev. C **84**, 045805 (2011).

[64] E. Aprile *et al.* (XENON), Phys. Rev. Lett. **119**, 181301 (2017), arXiv:1705.06655 [astro-ph.CO].

[65] D. S. Akerib *et al.*, arXiv (2016), arXiv:1608.05381 [physics.ins-det].

[66] D. S. Akerib *et al.* (LUX Collaboration), Phys. Rev. Lett. **118**, 021303 (2017).

[67] D. Huang, *Ultra-Low Energy Calibration of the LUX and LZ Dark Matter Detectors*, Ph.D. thesis, Brown U. (2020).

[68] D. S. Akerib *et al.*, "Improved Dark Matter Search Sensitivity Resulting from LUX Low-Energy Nuclear Recoil Calibration," (2022).

[69] E. Aprile, M. Anthony, Q. Lin, Z. Greene, P. de Perio, F. Gao, J. Howlett, G. Plante, Y. Zhang, and T. Zhu, Physical Review D **98** (2018), 10.1103/physrevd.98.112003.

[70] B. Lenardo, J. Xu, S. Pereverzev, O. A. Akindele, D. Naim, J. Kingston, A. Bernstein, K. Kazkaz, M. Tripathi, C. Awe, L. Li, J. Runge, S. Hedges, P. An,

and P. S. Barbeau, "Measurement of the ionization yield from nuclear recoils in liquid xenon between 0.3 – 6 keV with single-ionization-electron sensitivity," (2019), arXiv:1908.00518 [physics.ins-det].
[71] M. Horn *et al.*, Physics Letters B **705**, 471–476 (2011).
[72] P. Sorensen *et al.*, PoS **IDM2010**, 017 (2011), arXiv:1011.6439 [astro-ph.IM].
[73] P. Sorensen and C. E. Dahl, Physical Review D **83** (2011), 10.1103/physrevd.83.063501.
[74] C. Faham, V. Gehman, A. Currie, A. Dobi, P. Sorensen, and R. Gaitskell, Journal of Instrumentation **10**, P09010 (2015).
[75] B. Edwards *et al.*, JINST **13**, P01005 (2018), arXiv:1710.11032 [physics.ins-det].
[76] J. Xu, S. Pereverzev, B. Lenardo, J. Kingston, D. Naim, A. Bernstein, K. Kazkaz, and M. Tripathi, Phys. Rev. D **99**, 103024 (2019), arXiv:1904.02885 [physics.ins-det].
[77] J. Lindhard, Mat. Fys. Medd. K. Dan. Vidensk. Selsk. **33** (1963).
[78] P. Sorensen, Physical Review D **91** (2015), 10.1103/physrevd.91.083509.
[79] E. Aprile *et al.*, Physical Review Letters **123** (2019), 10.1103/physrevlett.123.241803.
[80] J. Birks, *The Theory and Practice of Scintillation Counting*, International Series of Monographs in Electronics and Instrumentation (Pergamon, 1964).
[81] A. Hitachi, Astroparticle Physics **24**, 247 (2005).
[82] E. Aprile, C. E. Dahl, L. de Viveiros, R. J. Gaitskell, K. L. Giboni, J. Kwong, P. Majewski, K. Ni, T. Shutt, and M. Yamashita, Phys. Rev. Lett. **97**, 081302 (2006).
[83] U. Fano, Phys. Rev. **72**, 26 (1947).
[84] G. Plante, *The XENON100 Dark Matter Experiment: Design, Construction, Calibration and 2010 Search Results with Improved Measurement of the Scintillation Response of Liquid Xenon to Low-Energy Nuclear Recoils*, Ph.D. thesis, Columbia U. (main) (2012).
[85] D. Akerib, S. Alsum, H. Araújo, X. Bai, J. Balajthy, P. Beltrame, E. Bernard, A. Bernstein, T. Biesiadzinski, E. Boulton, and et al., Physical Review Letters **122** (2019), 10.1103/physrevlett.122.131301.
[86] L. Wang and D. M. Mei, J. Phys. G **44**, 055001 (2017), arXiv:1604.01083 [physics.ins-det].
[87] D. S. Akerib *et al.* (LUX), Phys. Rev. Lett. **112**, 091303 (2014), arXiv:1310.8214 [astro-ph.CO].
[88] E. Aprile *et al.*, Physical Review D **102** (2020), 10.1103/physrevd.102.072004.
[89] D.-M. Mei, Z.-B. Yin, L. Stonehill, and A. Hime, Astroparticle Physics **30**, 12–17 (2008).
[90] P. Sorensen *et al.*, Nuclear Instruments and Methods in Physics Research Section A: Accelerators, Spectrometers, Detectors and Associated Equipment **601**, 339–346 (2009).
[91] W. Mu, X. Xiong, and X. Ji, "Scintillation efficiency for low-energy nuclear recoils in liquid-xenon dark matter detectors," (2013), arXiv:1306.0170 [physics.ins-det].
[92] F. Bezrukov, F. Kahlhoefer, and M. Lindner, Astroparticle Physics **35**, 119–127 (2011).
[93] W. Mu and X. Ji, "Ionization yield from nuclear recoils in liquid-xenon dark matter detection," (2013), arXiv:1310.2094 [physics.ins-det].
[94] Y. Sarkis, A. Aguilar-Arevalo, and J. C. D'Olivo, Physical Review D **101** (2020), 10.1103/physrevd.101.102001.
[95] B. Lenardo, K. Kazkaz, A. Manalaysay, J. Mock, M. Szydagis, and M. Tripathi, IEEE Trans. Nucl. Sci. **62**, 3387 (2015), arXiv:1412.4417 [astro-ph.IM].
[96] P. Sorensen, Nuclear Instruments and Methods in Physics Research Section A: Accelerators, Spectrometers, Detectors and Associated Equipment **635**, 41 (2011).
[97] A. Mozumder, Chemical Physics Letters **238**, 143 (1995).
[98] D. S. Akerib *et al.* (LUX), Phys. Rev. Lett. **116**, 161301 (2016), arXiv:1512.03506 [astro-ph.CO].
[99] J. Albert *et al.* (EXO-200), Phys. Rev. C **95**, 025502 (2017), arXiv:1609.04467 [physics.ins-det].
[100] J. Albert *et al.* (EXO-200), Phys. Rev. C **92**, 045504 (2015), arXiv:1506.00317 [nucl-ex].
[101] J. Verbus *et al.*, Nucl. Instrum. Meth. A **851**, 68 (2017), arXiv:1608.05309 [physics.ins-det].
[102] V. N. Lebedenko *et al.*, Phys. Rev. **D80**, 052010 (2009), arXiv:0812.1150 [astro-ph].
[103] E. Aprile *et al.*, "Search for New Physics in Electronic Recoil Data from XENONnT," (2022).
[104] J. Angle *et al.* (XENON), Phys. Rev. Lett. **100**, 021303 (2008), arXiv:0706.0039 [astro-ph].
[105] M. Szydagis *et al.* (LUX), in *10th International Symposium on Cosmology and Particle Astrophysics* (2014) arXiv:1402.3731 [hep-ex].
[106] D. S. Akerib *et al.* (LUX), Phys. Rev. **D97**, 102008 (2018), arXiv:1712.05696 [physics.ins-det].
[107] D. S. Akerib *et al.*, Nucl. Instrum. Meth. **A675**, 63 (2012), arXiv:1111.2074 [physics.data-an].
[108] D. S. Akerib *et al.* (LUX), Phys. Rev. **D97**, 112002 (2018), arXiv:1802.06162 [physics.ins-det].
[109] D. S. Akerib *et al.*, Physical Review D **101** (2020), 10.1103/physrevd.101.042001.
[110] J. R. Verbus, *An Absolute Calibration of Sub-1 keV Nuclear Recoils in Liquid Xenon Using D-D Neutron Scattering Kinematics in the LUX Detector*, Ph.D. thesis, Brown U. (2016).
[111] D. S. Akerib *et al.*, "Fast and flexible analysis of direct dark matter search data with machine learning," (2022).
[112] D. Akerib *et al.* (LUX Collaboration), Phys. Rev. D **96**, 112009 (2017), arXiv:1708.02566 [physics.ins-det].
[113] S. Agostinelli *et al.*, Nuclear Instruments and Methods in Physics Research Section A: Accelerators, Spectrometers, Detectors and Associated Equipment **506**, 250 (2003).
[114] J. Allison *et al.*, IEEE Trans. Nucl. Sci. **53**, 270 (2006).
[115] H. Araújo, "Revised performance parameters of the ZEPLIN-III dark matter experiment," (2020), arXiv:2007.01683 [physics.ins-det].
[116] N. Priel, L. Rauch, H. Landsman, A. Manfredini, and R. Budnik, JCAP **05** (2017), 10.1088/1475-7516/2017/05/013, arXiv:1610.02643 [physics.data-an].
[117] A. L. Fitzpatrick, W. Haxton, E. Katz, N. Lubbers, and Y. Xu, JCAP **1302**, 004 (2013), arXiv:1203.3542 [hep-ph].
[118] K. Arisaka, P. Beltrame, C. Ghag, K. Lung, and P. Scovell, Astroparticle Physics **37**, 51 (2012).
[119] D. S. Akerib *et al.*, Physical Review D **104** (2021), 10.1103/physrevd.104.062005.
[120] E. Aprile *et al.* (XENON Collaboration), Phys. Rev. Lett. **123**, 251801 (2019).
[121] R. F. Lang, A. Brown, E. Brown, M. Cervantes, S. Macmullin, D. Masson, J. Schreiner, and H. Simgen, JINST **11**, P04004 (2016), arXiv:1602.01138 [physics.ins-det].

[122] J. Aalbers *et al.*, "A next-generation liquid xenon observatory for dark matter and neutrino physics," (2022).

[123] D. Akerib, C. Akerlof, S. Alsum, H. Araújo, M. Arthurs, X. Bai, A. Bailey, J. Balajthy, S. Balashov, D. Bauer, and et al., Physical Review D **101** (2020), 10.1103/physrevd.101.052002.

[124] B. J. Mount *et al.* (LZ Collaboration), arXiv (2017), arXiv:1703.09144.

[125] D. S. Akerib *et al.* (LUX Collaboration), Nucl.Instrum.Meth. **A668**, 1 (2012), arXiv:1108.1836 [astro-ph.IM].

[126] D. S. Akerib *et al.* (LUX Collaboration), Nucl.Instrum.Meth. **A818**, 57 (2016), arXiv:1511.03541 [physics.ins-det].

[127] P. Sorensen, *A Position-Sensitive Liquid Xenon Time-Projection Chamber for Direct Detection of Dark Matter: The XENON10 Experiment*, Ph.D. thesis, Brown University (2008).

[128] L. de Viveiros, *Optimization of Signal versus Background in Liquid Xe Detectors Used for Dark Matter Direct Detection Experiments*, Ph.D. thesis, Brown University (2010).

[129] J. Aalbers *et al.*, "First Dark Matter Search Results from the LUX-ZEPLIN (LZ) Experiment," (2022).

[130] T. Pershing, D. Naim, B. Lenardo, J. Xu, J. Kingston, E. Mizrachi, V. Mozin, P. Kerr, S. Pereverzev, A. Bernstein, and M. Tripathi, "Calibrating the scintillation and ionization responses of xenon recoils for high-energy dark matter searches," (2022).

[131] W. H. Lippincott, K. J. Coakley, D. Gastler, A. Hime, E. Kearns, D. N. McKinsey, J. A. Nikkel, and L. C. Stonehill, Phys. Rev. C **78**, 035801 (2008).

[132] C. Amole *et al.* (PICO Collaboration), Phys. Rev. Lett. **118**, 251301 (2017).

[133] G. R. C. Rischbieter, meetings.aps.org/ Meeting/APR20/Session/R13.2 (April 2020 APS Meeting).

[134] E. Aprile *et al.* (XENON), Phys. Rev. D **100**, 052014 (2019), arXiv:1906.04717 [physics.ins-det].

[135] K. Ueshima *et al.*, Nuclear Instruments and Methods in Physics Research Section A: Accelerators, Spectrometers, Detectors and Associated Equipment **659**, 161 (2011).

[136] D. S. Akerib *et al.*, ArXiv e-prints (2015), arXiv:1509.02910 [physics.ins-det].

[137] J. Aalbers *et al.* (DARWIN), JCAP **11**, 017 (2016), arXiv:1606.07001 [astro-ph.IM].

[138] F. Kuger, "Charge signal measurement by scintillation in liquid xenon," (ECFA TF2 Symposium, April 09 2021).

[139] D. S. Akerib *et al.*, Phys. Rev. D **102**, 092004 (2020).

[140] J. Mock, N. Barry, K. Kazkaz, M. Szydagis, M. Tripathi, S. Uvarov, M. Woods, and N. Walsh, JINST **9**, T04002 (2014), arXiv:1310.1117 [physics.ins-det].

[141] J. Kwong, P. Brusov, T. Shutt, C. Dahl, A. Bolozdynya, and A. Bradley, Nuclear Instruments and Methods in Physics Research Section A: Accelerators, Spectrometers, Detectors and Associated Equipment **612**, 328 (2010).

[142] K. Abe *et al.*, Physical Review Letters **113** (2014), 10.1103/physrevlett.113.121301.

[143] E. Hogenbirk, M. Decowski, K. McEwan, and A. Colijn, JINST **13**, P10031 (2018), arXiv:1807.07121 [physics.ins-det].

[144] S. Kubota, A. Nakamoto, T. Takahashi, T. Hamada, E. Shibamura, M. Miyajima, K. Masuda, and T. Doke, Phys. Rev. B **17**, 2762 (1978).

[145] J. Dawson, A. Howard, D. Akimov, H. Araújo, A. Bewick, D. Davidge, W. Jones, M. Joshi, V. Lebedenko, I. Liubarsky, J. Quenby, G. Rochester, D. Shaul, T. Sumner, and R. Walker, Nuclear Instruments and Methods in Physics Research Section A: Accelerators, Spectrometers, Detectors and Associated Equipment **545**, 690 (2005).

[146] B. Adams, A. Elagin, H. Frisch, R. Obaid, E. Oberla, A. Vostrikov, R. Wagner, J. Wang, and M. Wetstein, Nuclear Instruments and Methods in Physics Research Section A: Accelerators, Spectrometers, Detectors and Associated Equipment **795**, 1 (2015).

[147] L. Baudis, P. Sanchez-Lucas, and K. Thieme, The European Physical Journal C **81** (2021), 10.1140/epjc/s10052-021-09834-x.

[148] R. Acciarri *et al.*, Journal of Instrumentation **8**, P08005 (2013).

[149] The KamLAND-Zen Collaboration, "First Search for the Majorana Nature of Neutrinos in the Inverted Mass Ordering Region with KamLAND-Zen," (2022).

[150] J. B. Albert *et al.* (nEXO Collaboration), Phys. Rev. C **97**, 065503 (2018).

[151] D. S. Akerib *et al.*, Physical Review C **102** (2020), 10.1103/physrevc.102.014602.

[152] E. Aprile *et al.* (XENON Collaboration), Phys. Rev. C **106**, 024328 (2022).

[153] G. Rutkai, M. Thol, R. Span, and J. Vrabec, Molecular Physics **115**, 1104 (2017), https://doi.org/10.1080/00268976.2016.1246760.

[154] M. Szydagis *et al.*, "Noble element simulation technique," (2022).